

# PCCP

Accepted Manuscript



This is an *Accepted Manuscript*, which has been through the Royal Society of Chemistry peer review process and has been accepted for publication.

*Accepted Manuscripts* are published online shortly after acceptance, before technical editing, formatting and proof reading. Using this free service, authors can make their results available to the community, in citable form, before we publish the edited article. We will replace this *Accepted Manuscript* with the edited and formatted *Advance Article* as soon as it is available.

You can find more information about *Accepted Manuscripts* in the [Information for Authors](#).

Please note that technical editing may introduce minor changes to the text and/or graphics, which may alter content. The journal's standard [Terms & Conditions](#) and the [Ethical guidelines](#) still apply. In no event shall the Royal Society of Chemistry be held responsible for any errors or omissions in this *Accepted Manuscript* or any consequences arising from the use of any information it contains.

## ARTICLE

# Interaction of Hydrogen with the Iron and Iron Carbide Interfaces: A ReaxFF Molecular Dynamics Study<sup>†</sup>

Cite this: DOI: 10.1039/x0xx00000x

Md Mahbubul Islam,<sup>a,b</sup> Chenyu Zou,<sup>b</sup> Adri C. T. van Duin,<sup>b,c</sup> and Sumathy Raman<sup>\*d</sup>Received 00th January 2012,  
Accepted 00th January 2012

DOI: 10.1039/x0xx00000x

www.rsc.org/

Hydrogen embrittlement (HE) is a well-known material phenomenon that causes significant loss in the mechanical strength of structural iron and often leads to catastrophic failures. In order to provide a detailed atomistic description of HE we have used a reactive bond order potential to describe adequately the diffusion of hydrogen as well as its chemical interaction with other hydrogen atoms, defects, and the host metal. The currently published ReaxFF force field for Fe/C/H systems was originally developed to describe Fischer-Tropsch (FT) catalysis [C. Zou, A. C. T. van Duin and D. C. Sorescu, *Top. Catal.*, 2012, 55, 391–401] and had been especially trained for surface formation energies, binding energies of small hydrocarbon radicals on different surfaces of iron and the barrier heights of surface reactions. We merged this force field with the latest ReaxFF carbon parameters [S. Goverapet Srinivasan, A. C. T. van Duin and P. Ganesh, *J. Phys. Chem. A*, 2015, 119, 1089–5639] and used the same training data set to refit the Fe/C interaction parameters. The present work is focused on evaluating the applicability of this reactive force field to describe material characteristics, and to study the role of defects and impurities in the bulk and at the precipitator interfaces. We study the interactions of hydrogen with pure and defective  $\alpha$ -iron (ferrite), Fe<sub>3</sub>C (cementite), and ferrite-cementite interfaces with a vacancy cluster. We also investigate the growth of nano voids in  $\alpha$ -iron using a grand canonical Monte Carlo (GCMC) scheme. The calculated hydrogen diffusion coefficients for both ferrite and cementite phases predict a decrease in the work of separation with increasing hydrogen concentration at a ferrite-cementite interface, suggesting a hydrogen-induced decohesion behavior. Hydrogen accumulation at the interface was observed during molecular dynamics (MD) simulations, which is consistent with experimental findings. These results demonstrate the ability of the ReaxFF potential to elucidate various aspects of hydrogen embrittlement in  $\alpha$ -iron and hydrogen interaction at a more complex metal/metal carbide interface.

## 1. Introduction

Hydrogen is well known for its deleterious effect on mechanical properties of metals and alloys.<sup>1–4</sup> In metallic systems, such as carbon steels, the presence of hydrogen often embrittles the material, a phenomenon known as hydrogen embrittlement (HE). The structural iron used in refinery industries and in oil and gas pipelines are particularly susceptible to HE due to their exposure to the hydrogen-rich environment. HE has received an enormous amount of research attention over the last few decades.<sup>5–7</sup> Many mechanisms have been proposed to explain HE. The inclusion of a few parts per million (ppm) of hydrogen in carbon steels can dramatically reduce fracture stress, strain, and ductility while also enhances brittleness, these often leads to disastrous brittle failure without plastic strain.<sup>8,9</sup> A hydrogen-induced delayed fracture mechanism has also been proposed, wherein the presence of hydrogen is known to initiate a crack in the material at an applied load that is lower than the yield stress of the material.<sup>10</sup> Beachem<sup>11</sup> suggests that subcritical crack growth in the material due to localized plastic deformation is prompted by the interaction of hydrogen with dislocations. The hydrogen-enhanced localized plasticity (HELP) theory predicts material failure due to the hydrogen-induced high mobility of dislocations, resulting in an increased local plasticity and agglomeration of dislocations, leading

to a plastic failure.<sup>12</sup> The mechanism of hydrogen enhanced decohesion (HEDE) has also been discussed widely as a mechanism for embrittlement in structural iron.<sup>13,14</sup> HEDE postulates that the accumulation of hydrogen in the lattice sites weakens the bonding strength between atoms of the host metal and reduces the material strength. The Griffith criteria suggests that the presence of hydrogen lowers surface energy and accelerates cleavage-like failures along the crystal planes of the material. HEDE damage occurs in crack tips and interfaces, where the presence of hydrogen lowers atomic cohesive strength and initiates interfacial debonding; consequently, cracks propagate at a lower applied tensile loading.<sup>15</sup> In general, these proposed models explain certain aspects of HE; however, a comprehensive mechanism has not been derived so far.<sup>6,16–18</sup>

Hydrogen inclusion in a material may happen during manufacturing, processing, or when the material is exposed to a hydrogen rich environment during its service life. Hydrogen traps at various lattice defects — dislocations, microvoids, grain boundaries, and precipitator interfaces — result in an increased amount of dissolved hydrogen in carbon steels. This is due to the fact that the trapping sites are generally lower in energy than the regular lattice sites.<sup>19,20</sup> Once introduced in the bulk iron, hydrogen diffuses quickly through the tetrahedral interstitial sites until it finds a trap or a surface such as a

vacancy or an interface.<sup>15</sup> Therefore, the processes of hydrogen trapping and diffusion in metallic materials are considered to be important elementary steps for developing an improved understanding of the mechanisms of HE.

Furthermore, numerous reports suggest that the inclusion of various non-metallic phases in high-strength carbon steel plays a significant role in the process of HE and in determining mechanical properties of the materials. Non-metallic precipitators may act as a strong trapping site and a retardant for the diffusing hydrogen atoms.<sup>10</sup> Hydrogen trapping at an interface could impact the decohesion of the host metal and initiate a crack.<sup>6</sup> Chan et al.<sup>21</sup> reported that the ferrite-cementite interfaces are dominant trapping sites for hydrogens owing to a relatively lower interfacial energy. Ramunni et al.<sup>22</sup> described the cementite phase as a major trapping site for hydrogen. Lee and co-workers<sup>23,24</sup> studied hydrogen trapping by TiC particles and the activation energy for the trapping of hydrogen. Other researchers<sup>25,26</sup> suggest that the presence of inclusions introduces voids, increases hydrogen concentration in the voids, and supports the growth of voids under the application of tensile loading. Consequently, crack initiation and propagation happens along the inclusion-metal interfaces.

Despite a great deal of research effort to explain the interaction of hydrogen with structural steel, a detailed understanding at an atomistic level has not been fully developed. The high mobility and low solubility of hydrogen in  $\alpha$ -iron impedes experimental techniques to offer a detailed characterization of the hydrogen interaction.<sup>27</sup> In this regard, atomistic simulations can effectively assist to probe different proposed hypotheses to gain insight into the underlying mechanism of HE on a length and time scale that is not accessible in experiments. Both the *ab-initio* and the classical molecular dynamics simulations have been employed in studying the iron-hydrogen systems. The static Density Functional Theory (DFT)-based *ab-initio* calculations focus primarily on ground-state energies of elementary steps to derive an understanding of the reaction paths as well as barriers of the reaction steps for hydrogen interactions with  $\alpha$ -iron while the classical simulations based on non-reactive force field focused on predicting the mechanical properties and the impact of hydrogen. Many atomistic simulation studies on iron-hydrogen systems are available in the literature, such as diffusion of hydrogen through bulk iron,<sup>28–31</sup> the trapping of hydrogen at vacancies,<sup>32–34</sup> and hydrogen accumulation at the crack tips.<sup>2</sup>

Moreover, the literature shows that efforts were made to implement a kinetic Monte Carlo (KMC) scheme to simulate the time evolution of a complex phenomenon like HE from the list of elementary steps together with their rates being identified using the high level DFT calculations.<sup>35,36</sup> Such a scheme is attractive and advantageous as it provides a more fundamental insight if the list of transitions in the transition table is complete. The latter is more challenging, especially when it involves surfaces and interfaces. In addition, owing to the complexity of the interfacial structures, no *ab-initio* or classical molecular dynamics studies have been conducted on hydrogen interaction with a ferrite-cementite interface. In this regard, the ReaxFF method is an attractive option as it is computationally less demanding compared to the *ab-initio* MD and/or the efforts needed upfront to explore the detailed DFT based potential energy surface for a KMC simulation. In addition, ReaxFF has demonstrated its ability to describe complex interfaces in a number of studies.<sup>37–39</sup>

In this study, we employed the ReaxFF reactive force field method to investigate vacancy-hydrogen interaction in a bulk  $\alpha$ -iron phase, the interaction of hydrogen at the ferrite-cementite interfaces, and void nucleation and growth of nanovoids in the  $\alpha$ -iron. In addition, this

work also explores the applicability of the Fe/C/H ReaxFF force field—which was originally developed and recently updated against the training set to describe elementary reactions in Fischer-Tropsch catalysis<sup>40</sup>—to investigate the chemistry of hydrogen interaction with the bulk iron and at the interfaces of ferrite-cementite phases.

The next section briefly describes the ReaxFF formalism and is followed by force field validation results for pure and defective iron, as well as for the  $\alpha$ -iron and Fe<sub>3</sub>C surfaces. Subsequent sections highlight the molecular dynamics simulation results on the diffusion of hydrogen in bulk  $\alpha$ -iron and Fe<sub>3</sub>C phases, growth of nanovoids, and hydrogen interaction with  $\alpha$ -iron in presence of a nanovoid and at interfaces

## 2. ReaxFF Background and Force Field Description

ReaxFF is a general bond order<sup>41,42</sup> (BO) based empirical force field method which allows bond breaking and formation in a dynamic simulation. The general form of the ReaxFF energy is shown below:

$$E_{\text{system}} = E_{\text{bond}} + E_{\text{over}} + E_{\text{under}} + E_{\text{lp}} + E_{\text{val}} + E_{\text{tor}} + E_{\text{vdWaals}} + E_{\text{Coulomb}}$$

It includes, respectively, partial energy contributions from the bond, over-coordination penalty and under-coordination stability, lone pair, valence, and torsion, non-bonded interactions van der Waals, and Coulomb energies.

ReaxFF uses the concept of bond orders to determine the bonded interactions among all atoms in a system. BO is a continuous function of distance between bonded atoms and accounts for contributions from sigma, pi, and double-pi bonds using the following expression.

$$\begin{aligned} BO'_{ij} &= BO_{ij}^{\sigma} + BO_{ij}^{\pi} + BO_{ij}^{\pi\pi} \\ &= \exp\left[p_{bo1} \cdot \left(\frac{r_{ij}}{r_o^{\sigma}}\right)^{p_{bo2}}\right] + \exp\left[p_{bo3} \cdot \left(\frac{r_{ij}}{r_o^{\pi}}\right)^{p_{bo4}}\right] \\ &\quad + \exp\left[p_{bo5} \cdot \left(\frac{r_{ij}}{r_o^{\pi\pi}}\right)^{p_{bo6}}\right] \end{aligned}$$

where  $BO_{ij}^{\sigma}$ ,  $BO_{ij}^{\pi}$ , and  $BO_{ij}^{\pi\pi}$  are the partial contributions of  $\sigma$ ,  $\pi$ - and double  $\pi$ -bonds between atoms  $i$  and  $j$ ,  $r_{ij}$  is the distance between  $i$  and  $j$ ,  $r_o^{\sigma}$ ,  $r_o^{\pi}$ , and  $r_o^{\pi\pi}$  are the bond radii of  $\sigma$ ,  $\pi$ - and double  $\pi$ -bonds, respectively, and  $p_{bo}$  terms are empirical parameters fit to either experimental or quantum data.

All of the connectivity-dependent interactions, i.e. the valence and torsion energy, are contingent on BO, therefore, as bond breaks their energy contribution also diminishes. Bonded and non-bonded interaction energies are calculated independently. Non-bonded interactions, i.e. the van der Waals and Coulomb, are calculated between every pair of atoms, regardless of their connectivity. Excessive repulsion at short distances is circumvented by adding a shielding parameter in non-bonded energy expressions and a 7<sup>th</sup> order taper function is used to eliminate any energy discontinuity.<sup>43,44</sup> The combination of covalent and Coulomb interactions enables ReaxFF to describe a wide range of systems, including covalent,<sup>45,46</sup> metallic,<sup>47</sup> metal hydride,<sup>48</sup> and carbide<sup>40</sup> systems. ReaxFF uses a geometry-dependent charge calculation scheme, the Electronegativity Equalization Method (EEM)<sup>49</sup> for charge calculation. ReaxFF method have been widely used to investigate a wide range of applications in materials,<sup>50–53</sup> catalysis<sup>54</sup>, and other chemical systems.<sup>55,56</sup> For a more

detailed description of the ReaxFF method, see van Duin et al.,<sup>46</sup> Chenoweth et al.,<sup>45</sup> and Russo Jr et al.,<sup>57</sup>

The original Fe/C/H ReaxFF force field<sup>40</sup> parameters were developed through extensive training against high-level quantum data for describing the equation of state of  $\alpha$ - and  $\gamma$ -phases of iron, and Fe<sub>3</sub>C, hydrogen interaction at different surfaces of  $\alpha$ -iron, surface formation energies of  $\alpha$ -iron and Fe<sub>3</sub>C<sub>2</sub>, binding energies of small hydrocarbon radicals on different surfaces of iron, and hydrogen dissolution in bulk iron at different concentrations. A detailed description of the force field development can be found in Ref.[40]. For this work, we retained the Fe/Fe and Fe/H parameters from the FT catalysis force field<sup>40</sup> and merged these with the recently developed ReaxFF carbon parameters.<sup>58</sup> Next, we performed refitting for Fe-C bond and 6 angle parameters, viz., Fe-C-Fe, H-C-Fe, C-Fe-C, C-Fe-H, C-H-Fe and C-H to restore the force field error to the same level as the original Fe/C/H force field.<sup>40</sup> This refitting was performed using the same training set data as used in ref.[1]. Key force field parameters are presented in Table I-IV. Detailed force field parameters are given in the supporting information.

One of the value added claims for any force field is transferability and this work demonstrates that the force field developed to address Fischer-Tropsch catalysis can be used to describe vacancies, vacancy migration, vacancy void formation and vacancy-hydrogen cluster formation in  $\alpha$ -iron and hydrogen interactions with the ferrite-cementite interfaces. While, the force field used in this study has been developed based on the two previously published work, none of those works evaluated the applicability of the force field for vacancy, hydrogen-vacancy interactions, interface energies, work of adhesion or diffusion of hydrogen.

Table I. Fe/C/H selected atom parameters

	$r_0$ (Å)	$\eta$ (eV)	$\chi$ (eV)	$\gamma$ (Å)	$p_{\text{ov/un}}$
Fe	1.9306	8.6241	1.7785	0.4744	-16.0573
C	1.3674	7.0000	4.8446	0.8485	-4.1021
H	0.8930	9.6093	3.7248	0.8203	-19.4571

For a definition of the parameters, see reference [46]

Table II. Fe/C/H selected bond parameters

	$D_e^\sigma$ (kcal/mol)	$p_{\text{be},1}$	$p_{\text{be},2}$	$p_{\text{bo},1}$	$p_{\text{bo},2}$	$p_{\text{kov}}$
Fe-Fe	44.2147	0.2236	0.4922	-0.0552	6.7583	0.2849
C-Fe	103.5536	0.8440	0.7522	-0.1509	4.0000	0.0100
H-Fe	78.2669	0.4668	0.5673	-0.1543	5.4965	0.1766

For a definition of the parameters, see reference [46]

Table III: Fe/C/H selected off diagonal bond parameters

	$D_{ij}$ (kcal/mol)	$R_{\text{vdW}}$ (Å)	$\alpha$	$r_0^\sigma$ (Å)
Fe-C	0.3999	1.4558	11.0036	1.3918
Fe-H	0.0200	1.9451	10.8595	1.4157
C-H	0.1200	1.3861	9.8561	1.1254

For a definition of the parameters, see reference [46]

Table IV. Fe/C/H selected angle parameters

	$\theta_0$ (degree)	$k_a$ (kcal/mol)	$k_b$ (1/rad) <sup>2</sup>	$p_{v,1}$	$p_{v,2}$
Fe-C-Fe	29.2204	18.5882	4.2644	0.0832	1.1249
H-C-Fe	0.3090	16.1111	1.4583	0.0100	1.4801
C-Fe-C	0.0100	39.5131	4.3816	0.5791	3.7111
C-Fe-H	48.0872	0.3787	0.0108	0.3648	1.5939
C-H-Fe	0.0100	2.8313	2.3314	2.7564	2.7554
Fe-C-H	0.3090	16.1111	1.4583	0.0100	1.4801

For a definition of the parameters, see reference [46]

### 3. Force Field Validation

In the present study, we performed a set of calculations to evaluate the capability of the Fe/C/H force field. Our objective was to investigate the interactions of hydrogen with the pure and defective bulk  $\alpha$ -iron, as well as at the ferrite-cementite interfaces. For this purpose, we evaluated our force field performance in a series of relevant cases and compared our calculated values with the data available in literature either from experiments or from high-level *ab-initio* computations.

#### 3.1 Bulk Properties of $\alpha$ -Iron and Fe<sub>3</sub>C

The bulk mechanical properties of  $\alpha$ -iron and Fe<sub>3</sub>C phases were investigated. In order to calculate the equilibrium lattice constants and the bulk moduli of both  $\alpha$ -iron and Fe<sub>3</sub>C, we performed simulations to obtain the energy-volume relationships. In this simulation, we applied both compression and expansion with respect to the equilibrium volume and recorded the corresponding energies. The equations of states as calculated from ReaxFF simulations and the corresponding DFT data for  $\alpha$ -iron<sup>59</sup> and Fe<sub>3</sub>C<sup>60</sup> are shown in Fig.1. The minimum of the energy-volume curve provides the equilibrium lattice constant and bulk modulus were calculated by fitting the data using Murnaghan equation of state. ReaxFF predicted equilibrium lattice constants of  $\alpha$ -iron and Fe<sub>3</sub>C are respectively:  $a=2.85\text{Å}$ , and  $a=5.09$ ,  $b=6.74$ ,  $c=4.53\text{Å}$ , which are in good agreement with the experimental data.<sup>61,62</sup> The bulk modulus values of the  $\alpha$ -iron and Fe<sub>3</sub>C phase as calculated from the Murnaghan equation of state are: 148 and 136 GPa, and they are in accordance with the reported literature value of 168<sup>62</sup> and 174±6 GPa,<sup>63</sup> respectively.

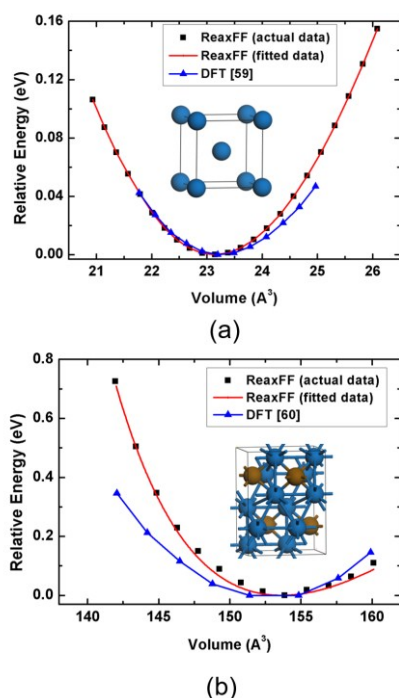


Fig. 1. Equation of states of (a)  $\alpha$ -iron and (b)  $\text{Fe}_3\text{C}$  phases as calculated using ReaxFF method and corresponding DFT values. Color scheme: carbon (ochre), and Iron (blue)

### 3.2 Hydrogen Binding and Diffusion in Bulk Iron

For the computation of hydrogen binding energies in bulk  $\alpha$ -iron, we considered an  $8 \times 8 \times 8$  supercell of the  $\alpha$ -iron. The bcc lattice has two high symmetry interstitial sites, namely, octahedral (O-site) and tetrahedral (T-site). It is well known that hydrogen dissolution in the bulk-iron is endothermic. Our calculated hydrogen dissolution energies are, respectively, 0.40 and 0.64 eV corresponding to the tetrahedral and octahedral sites. These values are in agreement with the data reported by other authors, such as 0.33-0.35 eV for the T-site,<sup>64</sup> and 0.43-0.55 eV for the O-site.<sup>31,65</sup> Hydrogen prefers to occupy the T-sites, and it is reported in the literature as the ground state for interstitial hydrogen,<sup>34</sup> while O-sites are not preferred due to the requirement of a larger lattice expansion to accommodate the hydrogen.<sup>31</sup> However, at elevated temperatures, hydrogen tends to occupy the octahedral sites. Jiang et al.<sup>31</sup> reported from their first principles calculations that the hydrogen dissolution energies at the T-sites are quite insensitive to the hydrogen concentration in the bulk-iron due to the absence of strong H-H interactions. Therefore, the presence of multiple hydrogens does not significantly affect the per hydrogen binding energy in the bulk-iron. Hydrogen diffusion barriers are also calculated for interstitial hopping. Two predominant diffusion pathways, such as T-T and T-O-T, are reported in literature. ReaxFF predicted diffusion barriers for T-T and T-O-T are, respectively, 0.032 and 0.3 eV, which are qualitatively consistent with the DFT calculated values of, respectively, 0.082 eV<sup>31</sup> and 0.19 eV.<sup>65</sup>

### 3.3 Vacancy Formation and Interaction with Hydrogen

A vacancy is a configuration in which an atom is missing from a regular lattice site. Vacancy plays an important role in Fe-H

interactions. We calculated a monovacancy formation energy as 2.5 eV, which is in agreement with the results from other DFT studies (1.95-2.76 eV)<sup>66-68</sup> and close to the reported experimental range of 1.6-2.1 eV.<sup>34,69</sup> The monovacancy formation energy was calculated using supercells of different sizes to eliminate the size effect. The vacancy migration barriers to the first and second nearest neighbors as calculated from the ReaxFF are, respectively, 0.83 eV and 2.95 eV, while the reported values in the literature are, respectively, 0.69 and 2.50 eV.<sup>69</sup> ReaxFF slightly overpredicts the vacancy migration barriers. It was observed that the presence of hydrogen in a lattice reduces vacancy formation energies.<sup>69</sup> The monovacancy formation energy in the vicinity of  $n$  hydrogen cluster is calculated using the following formula:

$$E_V^f = E(H_nV) - \frac{N-1}{N}E_0 - n[E(H_T) - E_0]$$

where,  $E(H_nV)$  is the energy with a vacancy-hydrogen cluster,  $N$  is the number of iron atoms in the perfect lattice with energy  $E_0$ ,  $n$  is the number of hydrogens, and  $E_T$  is the energy with a hydrogen atom at the T-site.

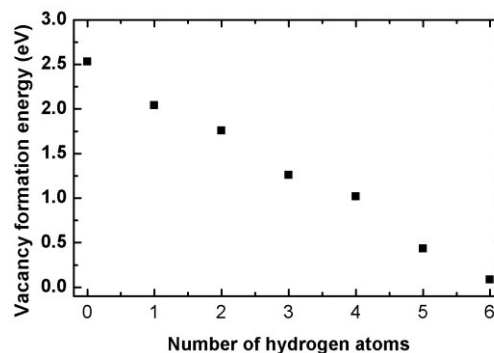


Fig. 2. Vacancy formation energies in presence of hydrogen clusters of various sizes in the vicinity of a monovacancy

ReaxFF predicts a systematic reduction in vacancy formation energies with the increasing number of hydrogens in the cluster that is consistent with previous DFT result.<sup>69</sup> Vacancy formation energy reduces to 0.08 eV in the presence of a cluster of six hydrogens around a monovacancy. ReaxFF predicted results of the vacancy formation energies in the presence of hydrogen clusters of various sizes are shown in Fig. 2.

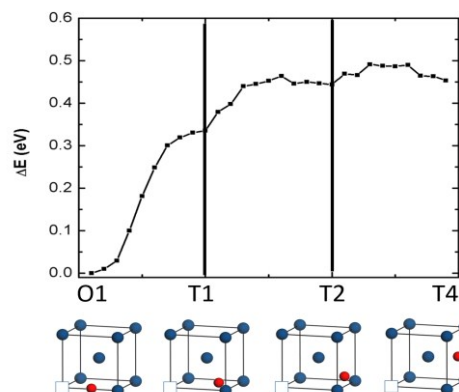


Fig. 3. The barriers to diffusion of a hydrogen-vacancy pair in bulk  $\alpha$ -iron. The hydrogen-vacancy pair configurations are shown schematically. White square and red sphere represent vacancy and hydrogen, respectively.

In a bcc-lattice, there are six possible sites around a monovacancy for trapping hydrogens. These sites are located near the octahedral sites of a bcc-lattice adjacent to the monovacancy as stated by Myers et al.<sup>70</sup> Vacancies form a strong trap for the hydrogen diffusing through the bulk. The incremental hydrogen trap energy in a monovacancy is calculated as:

$$E_{\text{trap}(m,n)} = [E(m,n-1) - E(0,m)] - [E(m,n) + E(0,0)]$$

where  $n$  and  $m$  are the number of hydrogens and vacancies, respectively. ReaxFF predicted hydrogen binding energies in a monovacancy site are tabulated in Table V. One can see that the ReaxFF results are in reasonable agreement with the available literature data.<sup>34</sup>

Table V. Hydrogen binding in a monovacancy site of  $\alpha$ -iron. For comparison results are shown from the previous DFT studies performed by Tateyama et al.<sup>36</sup>

Nr. of H	ReaxFF (eV)	Ref. [34] (eV)
1	0.50	0.55
2	0.45	0.51
3	0.50	0.40
4	0.32	0.27
5	0.24	0.33
6	-0.30	-0.019

We also calculated hydrogen diffusion barriers in the presence of a monovacancy. The energy barriers are calculated for hydrogen diffusion from one octahedral site to three other tetrahedral sites. The schematics of diffusion pathways are shown in Fig. 3 along with the corresponding relative energies. Comparison of the results with the DFT data from Hayward et al.<sup>69</sup> suggests a good agreement for the calculated energy barriers. All of these calculations establish the quality of the force field in predicting the vacancy-hydrogen interactions in  $\alpha$ -iron.

### 3.4 Surface Formation Energies of $\alpha$ -iron and Fe<sub>3</sub>C

We computed surface formation energies of both  $\alpha$ -iron and Fe<sub>3</sub>C and compared them with literature values. Three different  $\alpha$ -iron surfaces were considered in this study, namely, (110), (100), and (111). Surface formation energies were checked for the convergence with the number of layers, and in these computations, eight layers were found to be sufficient for the convergence in the energy within 0.01 Jm<sup>-2</sup>. Surface formation energies are calculated using the following relation:

$$\Delta E_s = \frac{1}{2A_s} (E_{\text{slab}} - nE_{\text{bulk}})$$

where,  $A_s$  is the surface area and  $E_{\text{slab}}$  and  $E_{\text{bulk}}$  are the energies of the slab and the bulk iron, respectively. ReaxFF predicted (110), (100), (111) surface formation energies are 2.15, 2.29, 2.59 Jm<sup>-2</sup>, respectively, while at the QM level, the values correspond to 2.29, 2.30, 2.59 Jm<sup>-2</sup>.<sup>71</sup> It can be seen that ReaxFF accurately reproduces the QM surface formation energies and the relative stability of each of the surfaces. ReaxFF predicted the (110) surface of  $\alpha$ -iron as the most stable surface and this is in agreement with the findings using high level quantum calculations.<sup>71</sup>

We considered three different Fe<sub>3</sub>C surfaces—(001), (010), and (100)—for surface formation energy calculations. Surface formation energies predicted by the ReaxFF for (001), (010), and (100) are, respectively, 2.06, 1.98, and 2.52 Jm<sup>-2</sup>, in close proximity with the

corresponding QM data<sup>72</sup> of 2.05, 2.26, and 2.47 Jm<sup>-2</sup>, respectively. However, the ReaxFF prediction of the lowest energy surface is in contradiction with the results from quantum computations.<sup>72</sup> ReaxFF calculations show nearly an equal stability for both the (001) and (010) surfaces, while the result from quantum computations directs the (001) surface as the lowest energy surface.

### 3.5 H-binding in Fe<sub>3</sub>C Surfaces

We carried out the DFT calculations for the binding energy of hydrogen at different Fe<sub>3</sub>C surfaces. The Vienna ab initio simulation package (VASP) was employed to solve Kohn-Sham equations with a plane-wave basis set.<sup>73,74</sup> We used Blöchl's all-electron frozen core projector augmented wave (PAW) method<sup>75</sup> to represent core electron regions with valence configurations of 3d<sup>7</sup> 4s<sup>1</sup> for Fe atoms and 1s<sup>1</sup> for H atoms and the generalized gradient approximation (GGA) of PBE was used to treat the exchange-correlation functional. A 15Å vacuum was introduced in the surface normal direction while periodic boundary condition was used in the other two directions. The atomic force convergence criterion for the structural optimizations was set as 0.05 eV Å<sup>-1</sup>. The Monkhorst-Pack (MP) Brillouin zone sampling method was used with a 9x11x10 k-point spacing and an energy cutoff of 450eV. In these calculations, zero point energy for the hydrogen was not considered. Our calculated DFT energies for the binding of a hydrogen atom at the (100), (010), and (001) surfaces are, respectively, -0.65, -0.60, and -0.46 eV, while the ReaxFF predicted energies are, respectively, -0.56, -0.67, and -0.57 eV. ReaxFF qualitatively reproduces DFT energies for the binding of hydrogen at the Fe<sub>3</sub>C surfaces considered in this study. Hydrogen binds at the three-folded sites of (100) and (010) surfaces, while for (001) surface hydrogen binds at a bridge site between two iron atoms. Three-fold binding sites are more stable than the bridge sites, and this is evident from the DFT energies as well. However, the ReaxFF predictions for the binding energies at the (100) and (010) surfaces are quite similar. In this study, it was important for the ReaxFF to capture the qualitative trend for hydrogen binding with the surfaces to describe the hydrogen interactions at the interfaces. For hydrogen binding data at the  $\alpha$ -iron surfaces, readers are referred to the ref. [40].

## 4. Results and Discussion

### 4.1 Hydrogen Diffusion Coefficients in Bulk $\alpha$ -iron and Fe<sub>3</sub>C

To calculate the diffusion coefficient of hydrogen in the bulk  $\alpha$ -iron, we performed NVT-MD simulations at various temperatures, such as, 300K, 400K, 500K, and 600K, with a temperature damping constant and a MD time step of 500 and 0.25 femtoseconds, respectively. Hydrogen atoms were randomly loaded in the bcc-lattice of iron at varying concentrations. Various system sizes and hydrogen concentrations were considered for this study. Supercell sizes of 8x8x8, 10x10x10, 14x14x14, and 18x18 x18 unit cells were chosen. The range of hydrogen concentration from 10<sup>-4</sup> to 10<sup>-2</sup> (hydrogen concentration is defined as the ratio of number of hydrogen to the number of iron atoms) was investigated. A periodic boundary condition was employed in all three directions. A conjugate gradient energy minimization scheme was used to perform the structural relaxation. During the MD simulations, trajectories were saved at every 0.125 picosecond. Diffusion coefficients were computed using the mean square displacement (MSD) of hydrogen atoms that was determined from the unfolded atomic coordinates after the system achieved

equilibrium at the simulation temperature. MSDs and diffusion coefficients (DCs) were calculated using the Einstein's relation:

$$MSD = \langle |r(t) - r(0)|^2 \rangle$$

$$D = \frac{1}{6} \lim_{\Delta t \rightarrow \infty} \frac{MSD(t + \Delta t) - MSD(t)}{\Delta t}$$

where  $r$  is the position of the particle,  $t$  is the time, and  $D$  is the diffusion coefficient.

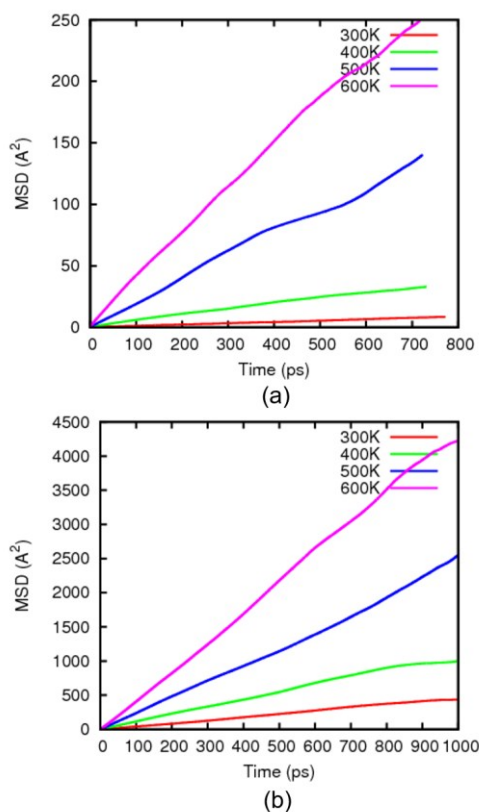


Fig. 4. MSD vs. time plot at various temperatures for diffusion of hydrogen in (a)  $\alpha$ -iron (b)  $Fe_3C$  phase

The apparent DC were calculated using the following Arrhenius equation:<sup>76</sup>

$$D(T) = D_0 \exp\left(-\frac{E_a}{kT}\right)$$

where  $D_0$  is the pre-exponential factor,  $E_a$  is the activation energy,  $k$  is the Boltzmann constant, and  $T$  is the temperature. The activation energy and the pre-exponential factors are independent of temperature and were computed using an exponential regression analysis of a  $D$  vs.  $1/T$  plot. Figure 4(a) shows MSD vs. time plot for the hydrogen concentration of  $10^{-2}$  in the bulk  $\alpha$ -iron. The statistical average of the diffusion coefficient results derived from ten different simulations at four different temperatures is shown in Fig. 5 with error bars. The mean hydrogen diffusion coefficient at 300K is calculated as  $7.1 \times 10^{-10} \text{ m}^2 \text{ s}^{-1}$ . ReaxFF underestimates the experimental diffusion coefficient by about 50% in comparison with the experimental data in [77]. The magnitude of this deviation can be attributed to the relatively higher hydrogen concentration considered in this study as well to the time-scales used in these

computations. Pre-exponential factors and activation barriers are calculated using least-square regression analysis. We represent the diffusion coefficient as a function of temperature with the following expression:  $D(T) = 5 \times 10^{-8} \exp(-1318/T) \text{ m}^2 \text{ s}^{-1}$ . The activation barrier for hydrogen diffusion is calculated as 0.11 eV. The activation barrier calculated from the MSD plot is relatively higher than the barrier calculated from the static calculation for the minimum energy diffusion pathway (T-T jump), which implies—H diffusion mechanism cannot be solely attributed to the T-T jump. Due to the temperature effect, T-O-T jump also has a finite probability. At a higher temperature, higher entropy also facilitates T-O-T jump. In addition, hydrogen-hydrogen interaction affects hydrogen diffusion barrier in our dynamic simulations.<sup>78</sup> The hydrogen diffusion mechanism in pure  $\alpha$ -iron can be attributed to the interstitial diffusion only—predominantly through the T-T site, however, T-O-T diffusion was also observed during the simulation.

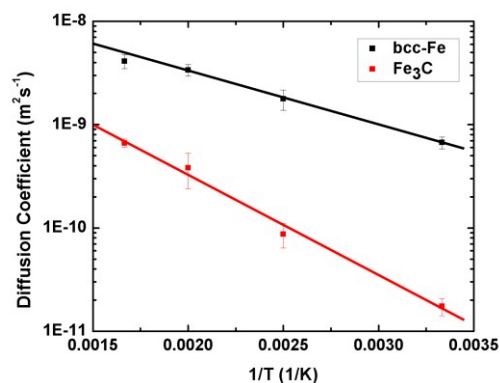


Fig. 5. Diffusion coefficient of hydrogen in the  $\alpha$ -iron and  $Fe_3C$  phases as a function of temperature (Y-axis is in logarithmic scale)

We also calculated the hydrogen diffusion coefficient at the  $Fe_3C$  phase following the same procedure described for the  $\alpha$ -iron simulations. The hydrogen concentration range was between  $10^{-4}$  -  $10^{-2}$  for the  $Fe_3C$ . ReaxFF predicted mean hydrogen diffusion coefficient in the  $Fe_3C$  at 300K is  $1.84 \times 10^{-11} \text{ m}^2 \text{ s}^{-1}$ , which is an order of magnitude slower than the corresponding  $\alpha$ -iron case. From the Arrhenius plot, the activation barrier and pre-exponential factor are calculated as 0.80 eV and  $3 \times 10^{-8} \text{ m}^2 \text{ s}^{-1}$ . The predicted higher activation barrier resulted in slower hydrogen diffusion in the  $Fe_3C$  phase. The calculated average diffusion coefficients at various temperature are shown in Fig. 5 along with error bars. The hydrogen diffusion coefficient as a function of temperature can be expressed as:  $D(T) = 3 \times 10^{-8} \exp(-2243/T) \text{ m}^2 \text{ s}^{-1}$ . Overall, the agreement between ReaxFF and the available literature demonstrates that the Fe/C/H potential can be used to derive hydrogen diffusion properties in the bulk  $\alpha$ -iron and  $Fe_3C$  over a range of temperatures and hydrogen concentrations.

#### 4.2 Void Nucleation and Growth in $\alpha$ -Iron

Structural materials exposed to the irradiation environment undergo changes in structure and physical properties. Irradiating particle displaces atoms from their lattice positions and creates vacancies and self-interstitial defects.<sup>79,80</sup> Iron structures of the fission and fusion reactors experience extreme radiation fields. However, the prediction of irradiation induced vacancies and their growth to form nanovoids requires a time scale (seconds to year), which is prohibitive for the

conventional MD methods.<sup>81</sup> Previously, KMC<sup>82</sup> and rate theory<sup>83</sup> were used to study the void growth; however, these methods depend heavily on the reaction rates and barriers derived from atomistic simulations. In this study, we employed a relatively simplified approach—the grand canonical Monte Carlo (GCMC) scheme<sup>84</sup>—to investigate the nucleation and formation of vacancy clusters. The migration of monovacancies and their combination with other vacancies leads to the formation of a vacancy cluster. The Metropolis criteria based swap move of the GCMC scheme enabled us to investigate vacancy cluster formation. An  $\alpha$ -iron 8x8x8 supercell is used for this simulation. The initial geometry contains 50 randomly distributed monovacancies. This high vacancy concentration represents a super-abundant vacancy configuration.<sup>29</sup>

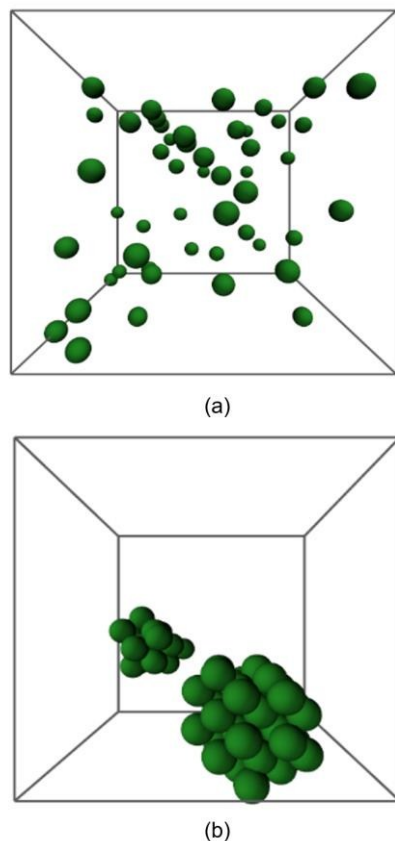


Fig. 6. Vacancy cluster formation during a GCMC simulation (a) initial vacancy distribution (b) formation of vacancy clusters (vacancies are represented as green sphere and lattice iron atoms are not shown for clarity)

A GCMC swap move was allowed only to swap a vacancy with a lattice site. The GCMC move was accepted when vacancy swapping is energetically favored. The results from this simulation are shown in Fig. 6. Large vacancy clusters comprising of 29 and 21 vacancies were observed during the GCMC move. Coalescence of the isolated vacancies to large vacancy clusters supports the experimental evidence of nanovoids formation in irradiated iron.<sup>85</sup>

#### 4.3 Diffusion of Hydrogen in Presence of a Vacancy Cluster

Hydrogen precipitation at dislocations and voids in the  $\alpha$ -iron is a well-known phenomenon.<sup>86</sup> Strong attraction of the hydrogen towards the defect sites is a cause of increased hydrogen concentration in the

voids. We performed MD simulations to study this phenomenon. We created a cubic lattice of 8x8x8 supercell of  $\alpha$ -iron, and a spherical void of 10Å diameter was introduced by removing lattice iron atoms. Twenty hydrogen atoms were randomly inserted in the simulation cell. Periodic boundary conditions were used in all three directions. After performing a structural relaxation simulation, we conducted a NVT-MD simulation at 500K with a temperature damping constant of 500fs. The simulation cell and the hydrogen trajectories from the MD simulation are shown in Fig. 7.

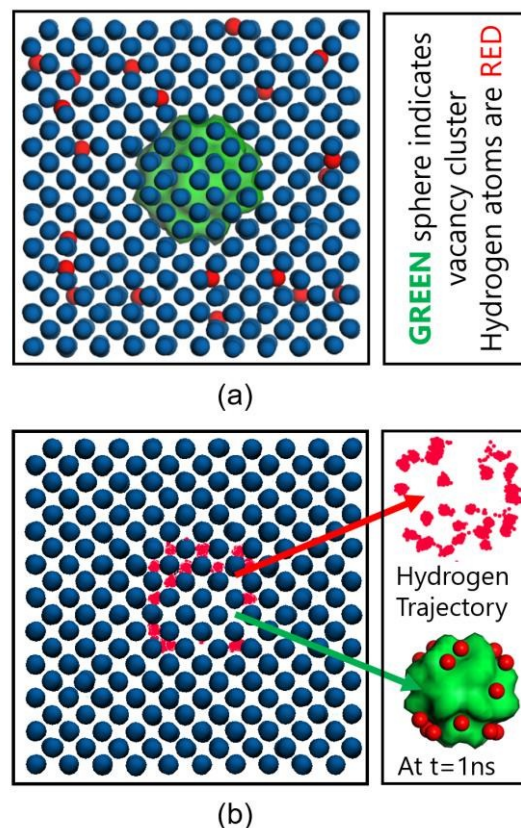


Fig. 7. Hydrogen binding at a vacancy cluster in a 500K NVT MD simulation, (a) Initial configuration, (b) Equilibrated hydrogen trajectories during this simulation. Color scheme: Iron (blue).

Hydrogen atoms diffused through the lattice, and once they arrived at the vacancy site they bonded with the inner surface. Hydrogen accumulation at the void inner surface was increased as simulation proceeded. Thus within 400ps of simulation, all the hydrogen atoms bonded at the vacancy site. This trapping of hydrogen at the vacancy cluster and an increased concentration of hydrogen at the void is consistent with the experimental observation of hydrogen induced blister formation in the pipeline steel.<sup>25</sup>

#### 4.4 Ferrite-Cementite Interface Simulations

Typically, interfaces are formed due to the presence of different precipitators in a structural iron. Commonly observed precipitators are Fe<sub>3</sub>C, Fe<sub>2</sub>C<sub>5</sub>, and TiC.<sup>24,87</sup> In this study, we considered the Fe<sub>3</sub>C precipitator in an  $\alpha$ -iron phase and investigated the interaction of hydrogens at interfaces and also with the individual phases. Interfaces were modeled by a slab, which consists of a finite number of layers of ferrite and cementite structure. In our slab model, we considered Bagarytsky interfaces (BI) that are commonly observed in the ferrite-

cementite system.<sup>88</sup> Two BIs are considered in this study, namely, C100/F1 $\bar{1}0$ , and C010/F111, where C and F represent cementite and ferrite surfaces, respectively. Surfaces were cut from the individual bulk phases, and we constructed surface supercells of both phases so that upon interface formation, lattice mismatch is minimized. Cell dimensions of C100/F1 $\bar{1}0$ , and C010/F111 interfaces were, respectively, 20.0 x 32.0 x 60.0 and 36.0 x 20.0 x 60.0Å. Lattice misfit for C100/F1 $\bar{1}0$ , and C010/F111 interfaces are, respectively, ~0.5% and ~3%. We constructed these interface geometries in the Materials studio 7. Periodic boundary conditions were employed in the y and z-directions while the x-direction was set as non-periodic (Fig 9).

In structural iron, adhesion between a precipitator and the metal interface plays a significant role in predicting their mechanical strength. Hydrogen accumulation at an interface enhances the tendency of embrittlement. It was experimentally observed that the presence of hydrogens at the interface weakens the bonding, thus leading to the propagation of decohesion-induced failure along the interfacial boundary.<sup>25</sup> To examine this effect, we performed a set of simulations where we placed hydrogen atoms at the interfaces at various concentrations and performed structural relaxation simulations using the conjugate gradient scheme.

The work of separation ( $W_{sep}$ ), as introduced by Finnis et al.<sup>89</sup> is vital for quantifying the interfacial adhesion.  $W_{sep}$  is defined as the reversible work needed to separate an interface into two free surfaces, which is a measure of the strength of the interfaces<sup>89</sup> and calculated as:

$$W_{sep} = \sigma_{Fe-sv} + \sigma_{Fe_3C-sv} - \sigma_{Fe/Fe_3C} \\ = (E_{Fe} + E_{Fe_3C} - E_{Fe/Fe_3C})/2A$$

where,  $\sigma_{Fe-sv}$ ,  $\sigma_{Fe_3C-sv}$  are the solid-vapor surface energies, and  $\sigma_{Fe/Fe_3C}$  is the interface energy;  $E_{Fe}$  and  $E_{Fe_3C}$  are the total energies for the iron, cementite slab, respectively.  $E_{Fe/Fe_3C}$  is the total energy of the slab model with interfaces, and A is the interfacial area.

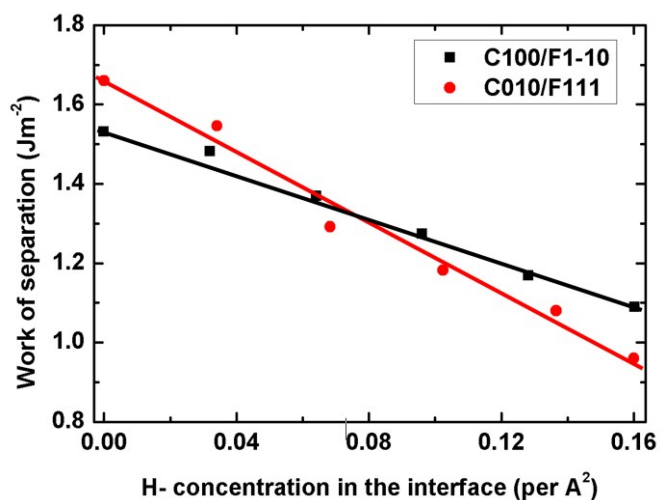


Fig. 8. Work of separation as a function of hydrogen concentration at the C100/F1 $\bar{1}0$  and C010/F111 Bagaryatskys' interfaces. C and F stands for cementite and ferrite surfaces, respectively.

We calculated  $W_{sep}$  for both of the BI interfaces at different hydrogen concentrations. Fig. 8 represents the relation between  $W_{sep}$  and

hydrogen concentrations at the interfaces. Note that the reported  $W_{sep}$  values do not account for the effect of uncertainty stemming from different arrangement of hydrogens. In the current approach, we begin with a random placement of hydrogens and rely on the optimizer to fully relax and minimize the structure. However, the optimizer could only ensure us to provide the nearby local minimum for a given initial geometry and not the global minimum. Alternatively, one could start with "n" different starting configurations and aim to arrive at an estimate of uncertainty by fully relaxing them. Since, the uncertainty thus calculated would still not reflect the true measure of it as there is no way to ensure that one has tried all possible arrangements of hydrogens. Consequently, our intent in Fig. 8 is not to provide a quantitative measure of  $W_{sep}$  instead to demonstrate qualitatively the trend in  $W_{sep}$  with increasing hydrogens at the interface. One can see that in Fig. 8 for both of the interfacial configurations,  $W_{sep}$  decreases with the increasing hydrogen concentration at the interfaces, which indicates the weakening of the interfaces—i.e. lower energy is needed to cleave the interface into two surfaces. This finding corroborates with the observation of the hydrogen induced decohesion at the interfaces.<sup>25</sup> Wang and co-workers<sup>90</sup> study on Cu/Al<sub>2</sub>O<sub>3</sub> interfaces also revealed hydrogen-assisted reduction in  $W_{sep}$ .

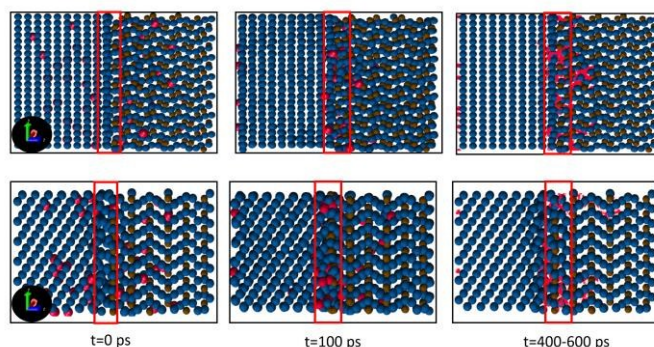


Fig. 9. Diffusivity and segregation of hydrogen at Bagaryatskys' Interfaces at  $t=0ps$ ,  $t=100ps$  and  $t=400-600ps$ . Top panel: C100/F1 $\bar{1}0$  and bottom panel: C010/F111. Color scheme: equilibrated hydrogen trajectories (red dots), hydrogen (red), carbon (ochre), and iron (blue).

Furthermore, hydrogen diffusion kinetics were studied in ferrite-cementite interface geometries. Twenty hydrogen atoms were randomly placed in each of the phases, and MD simulations were performed. The structural relaxation simulations followed by the NVT-MD simulations were performed at 500K temperature. *Fig. 9 shows the evolution of the diffusivity of hydrogen atoms at 0ps, 100ps and the trajectory of equilibrated hydrogen atoms (shown as red dots) for 400-600ps at both interfaces.* During the NVT-MD simulation, hydrogen atoms diffuse towards the interface from both phases and hydrogen accumulation is observed at the interface. The higher hydrogen diffusion coefficient at the ferrite phase facilitates the diffusion of hydrogen atoms to the interface at an expedited rate, while hydrogen segregation from the cementite phase to the interface takes place at a slower rate. Hanada *et al.*<sup>91</sup> reported that hydrogen atoms diffusing through the ferrite phase are being attracted to the cementite at the interface is also responsible for the hydrogen accumulation at the interfaces.<sup>91</sup> Our results on the hydrogen segregation at the interfaces are consistent with the experimental observation.<sup>91</sup> Diffusion coefficient of the hydrogen atoms—trapped at the interfaces—is found three order of magnitude slower than the bcc-iron phase. For example, diffusion coefficient of hydrogen atoms

trapped at the C010/F111 interface is calculated as  $2.40 \times 10^{-13} \text{ ms}^{-2}$ . Since interfaces act as a strong trap site for the hydrogen, we did not observe any hydrogen atoms to cross the interface from either of the phases.

## 5. Conclusions

We employed the Fe/C/H ReaxFF force field to explore experimentally observed phenomenon of hydrogen interaction with pure and defective  $\alpha$ -iron and with two types of Bagarytsky interfaces (BI) between the ferrite and cementite phases. ReaxFF simulations reasonably predict the diffusion coefficients of hydrogen in the  $\alpha$ -iron and Fe<sub>3</sub>C phases and hydrogen trapping at nanovoids. The prediction of phase dependent hydrogen diffusivity and hydrogen segregation at the interfaces agrees with experimental observations. The values of predicted hydrogen diffusion coefficient in three different phases follows a sequence of  $D_{\alpha\text{-iron}} > D_{\text{Fe}_3\text{C}} > D_{\text{interfaces}}$ . The Grand Canonical Monte Carlo (GCMC) simulation demonstrates the ability of the ReaxFF method in describing vacancy cluster formation and the growth of nanovoids. ReaxFF captures the phenomenon of hydrogen-induced decohesion type failures at the interfaces. Increase in hydrogen concentration at the interfaces reduces the work of separation, suggesting the possibility of crack propagation along the interfaces. Overall, the simulation results obtained in this study demonstrates that the Fe/C/H force field can satisfactorily describe hydrogen, vacancy, ferrite, and cementite interactions, which encourages us to extend our studies towards other aspects of hydrogen embrittlement using ReaxFF. Investigations are underway to explore the effect of hydrogen on the mechanical properties of iron nanowire and crack propagation behavior in  $\alpha$ -iron in the presence of hydrogen and precipitator interface. Most importantly, the present work highlights the transferability of the Fe/C/H force field that is trained against the data for describing Fischer-Tropsch catalysis to materials' characterization and emphasizes ReaxFF force field validation as a prerequisite while engaging ReaxFF capability for its unique strength to enable investigations of the effect of chemistry on the mechanical properties of the material. Additional work is in progress to extend the length scales of reactive MD to hundreds of nanometers by using an adaptive hybrid force field scheme that involves a computationally intensive ReaxFF reactive force field description for the complex surface chemistry and computationally less expensive Tersoff or EAM potential to adequately describe the mechanical properties of the material.

## Acknowledgments

This work was supported by the Corporate Strategic Research, ExxonMobil Research and Engineering, Clinton, NJ. We like to thank Srinivasan Rajagopalan, Neeraj Thirumalai, and Lili Gai for useful comments and discussions.

## Notes and References

<sup>a</sup>Summer Intern, ExxonMobil Research and Engineering, Annandale, New Jersey, 08801, USA

<sup>b</sup>Department of Mechanical and Nuclear Engineering, The Pennsylvania State University, University Park, PA 16802, USA

<sup>c</sup>RxFF\_Consulting, LLC, State College, PA 16801, USA

<sup>d</sup>ExxonMobil Research and Engineering, Annandale, New Jersey, 08801, USA

<sup>e</sup>Email: [sumathy.raman@exxonmobil.com](mailto:sumathy.raman@exxonmobil.com), Phone: (908) 730-2512, Fax: (908) 730-3323

<sup>f</sup>Electronic supplementary information (ESI) available. See DOI:

- 1 T. Doshida, H. Suzuki, K. Takai, N. Oshima and T. Hirade, *ISIJ Int.*, 2012, **52**, 198–207.
- 2 J. Song and W. A. Curtin, *Acta Mater.*, 2011, **59**, 1557–1569.
- 3 J. Song and W. A. Curtin, *Nat. Mater.*, 2013, **12**, 145–151.
- 4 S. P. Lynch, *Hydrog. Eff. Mater. Behav. Corros. Deform. Interact.*, 2003, 449–466.
- 5 Y. Fukai, *The metal-hydrogen system: basic bulk properties*, Springer Science & Business Media, 2006, vol. 21.
- 6 M. Nagumo, *Mater. Sci. Technol.*, 2004, **20**, 940–950.
- 7 A. Pundt and R. Kirchheim, *Annu. Rev. Mater. Res.*, 2006, **36**, 555–608.
- 8 J. P. Hirth, *Metall. Trans. A*, 1980, **11**, 861–890.
- 9 A. Rajabipour and R. E. Melchers, *Int. J. Hydrog. Energy*, 2015, **40**, 9388–9399.
- 10 M. Nagumo, T. Tamaoki and T. Sugawara, *Hydrog. Eff. Mater. Behav. Corros. Deform. Interact. NR Moody AW Thompson RE Ricker GW Was RH Jones Eds Miner. Met. Mater. Soc. N. Y.*, 2002, 999–1008.
- 11 C. D. Beachem, *Metall. Trans.*, 1972, **3**, 441–455.
- 12 H. K. Birnbaum and P. Sofronis, *Mater. Sci. Eng. A*, 1994, **176**, 191–202.
- 13 A. R. Troiano, *Trans ASM*, 1960, **52**, 54–80.
- 14 J. G. Morlet, H. H. Johnson and A. R. Troiano, *A new concept of hydrogen embrittlement in steel*, Wright Air Development Center, Air Research and Development Command, United States Air Force, 1957.
- 15 R. A. Oriani, *Acta Metall.*, 1970, **18**, 147–157.
- 16 H. C. Rogers, *Science*, 1968, **159**, 1057–1064.
- 17 K. H. Lo, C. H. Shek and J. K. L. Lai, *Mater. Sci. Eng. R Rep.*, 2009, **65**, 39–104.
- 18 H. Momida, Y. Asari, Y. Nakamura, Y. Tateyama and T. Ohno, *Phys. Rev. B*, 2013, **88**, 144107.
- 19 J. L. Lee and J. Y. Lee, *Met. Sci.*, 1983, **17**, 426–432.
- 20 W. Y. Choo and J. Y. Lee, *J. Mater. Sci.*, 1982, **17**, 1930–1938.
- 21 S. L. I. Chan and J. A. Charles, *Mater. Sci. Technol.*, 1986, **2**, 956–962.
- 22 V. P. Ramunni, T. D. P. Coelho and P. E. V. de Miranda, *Mater. Sci. Eng. A*, 2006, **435–436**, 504–514.
- 23 S. M. Lee and J. Y. Lee, *Acta Metall.*, 1987, **35**, 2695–2700.
- 24 H. G. Lee and J.-Y. Lee, *Acta Metall.*, 1984, **32**, 131–136.
- 25 H.-L. Lee and S. Lap-Ip Chan, *Mater. Sci. Eng. A*, 1991, **142**, 193–201.
- 26 S. Fujita and Y. Murakami, *Metall. Mater. Trans. A*, 2013, **44**, 303–322.
- 27 M. Wen, X.-J. Xu, S. Fukuyama and K. Yokogawa, *J. Mater. Res.*, 2001, **16**, 3496–3502.
- 28 A. Ramasubramaniam, M. Itakura, M. Ortiz and E. A. Carter, *J. Mater. Res.*, 2008, **23**, 2757–2773.
- 29 R. Nazarov, T. Hickel and J. Neugebauer, *Phys. Rev. B*, 2014, **89**, 144108.
- 30 D. Tanguy and M. Mareschal, *Phys. Rev. B*, 2005, **72**, 174116.
- 31 D. E. Jiang and E. A. Carter, *Phys. Rev. B*, 2004, **70**, 064102.
- 32 B. Irigoyen, R. Ferullo, N. Castellani and A. Juan, *J. Phys. Appl. Phys.*, 1996, **29**, 1306.
- 33 M. E. Pronsato, C. Pistonesi and A. Juan, *J. Phys. Condens. Matter*, 2004, **16**, 6907.
- 34 Y. Tateyama and T. Ohno, *Phys. Rev. B*, 2003, **67**, 174105.
- 35 Y. A. Du, J. Rogal and R. Drautz, *Phys. Rev. B*, 2012, **86**, 174110.
- 36 L. Ismer, T. Hickel and J. Neugebauer, *Phys. Rev. B*, 2010, **81**, 094111.
- 37 U. Khalilov, G. Pourtois, A. C. T. van Duin and E. C. Neyts, *J. Phys. Chem. C*, 2012, **116**, 21856–21863.
- 38 Q. Zhang, T. Çağın, A. van Duin, W. A. Goddard III, Y. Qi and L. G. Hector Jr, *Phys. Rev. B*, 2004, **69**, 045423.
- 39 B. V. Merinov, J. E. Mueller, A. C. T. van Duin, Q. An and W. A. Goddard, *J. Phys. Chem. Lett.*, 2014, 4039–4043.
- 40 C. Zou, A. C. T. van Duin and D. C. Sorescu, *Top. Catal.*, 2012, **55**, 391–401.
- 41 J. Tersoff, *Phys. Rev. Lett.*, 1988, **61**, 2879–2882.
- 42 D. W. Brenner, *Phys. Rev. B*, 1990, **42**, 9458–9471.
- 43 T. Liang, Y. K. Shin, Y.-T. Cheng, D. E. Yilmaz, K. G. Vishnu, O. Verners, C. Zou, S. R. Phillpot, S. B. Sinnott and A. C. T. van Duin, *Annu. Rev. Mater. Res.*, 2013, **43**, 109–129.
- 44 A. C. Van Duin, A. Strachan, S. Stewman, Q. Zhang, X. Xu and W. A. Goddard, *J. Phys. Chem. A*, 2003, **107**, 3803–3811.
- 45 K. Chenoweth, A. C. T. van Duin and W. A. Goddard, *J. Phys. Chem. A*, 2008, **112**, 1040–1053.

- 46 A. C. Van Duin, S. Dasgupta, F. Lorant and W. A. Goddard, *J. Phys. Chem. A*, 2001, **105**, 9396–9409.
- 47 M. R. LaBrosse, J. K. Johnson and A. C. T. van Duin, *J. Phys. Chem. A*, 2010, **114**, 5855–5861.
- 48 S. Cheung, W.-Q. Deng, A. C. T. van Duin and W. A. Goddard, *J. Phys. Chem. A*, 2005, **109**, 851–859.
- 49 W. J. Mortier, S. K. Ghosh and S. Shankar, *J. Am. Chem. Soc.*, 1986, **108**, 4315–4320.
- 50 O. Vernalis and A. C. T. van Duin, *Surf. Sci.*, 2015, **633**, 94–101.
- 51 M. M. Islam, A. Ostadhosseini, O. Borodin, A. T. Yeates, W. W. Tipton, R. G. Hennig, N. Kumar and A. C. T. van Duin, *Phys. Chem. Chem. Phys.*, 2015, **17**, 3383–3393.
- 52 A. Ostadhosseini, E. D. Cubuk, G. A. Tritsarlis, E. Kaxiras, S. Zhang and A. C. T. van Duin, *Phys. Chem. Chem. Phys.*, 2015.
- 53 C. Zou, Y. K. Shin, A. C. T. van Duin, H. Fang and Z.-K. Liu, *Acta Mater.*, 2015, **83**, 102–112.
- 54 C. Zou and A. V. Duin, *JOM*, 2012, **64**, 1426–1437.
- 55 M. M. Islam, V. S. Bryantsev and A. C. T. van Duin, *J. Electrochem. Soc.*, 2014, **161**, E3009–E3014.
- 56 D.-C. Yue, T.-B. Ma, Y.-Z. Hu, J. Yeon, A. C. van Duin, H. Wang and J. Luo, *Langmuir*, 2015, **31**, 1429–1436.
- 57 M. F. Russo Jr. and A. C. T. van Duin, *Nucl. Instrum. Methods Phys. Res. Sect. B Beam Interact. Mater. At.*, 2011, **269**, 1549–1554.
- 58 S. G. Srinivasan, A. C. T. van Duin and P. Ganesh, *J. Phys. Chem. A*, 2015, **119**, 571–580.
- 59 L. S. I. Liyanage, S.-G. Kim, J. Houze, S. Kim, M. A. Tschopp, M. I. Baskes and M. F. Horstemeyer, *Phys. Rev. B*, 2014, **89**, 094102.
- 60 W. G. Marshall, G. D. Price and I. G. Wooda, *Earth Planet. Sci. Lett.*, 2002, **203**, 575.
- 61 F. H. Herbstein and J. Smuts, *Acta Crystallogr.*, 1964, **17**, 1331–1332.
- 62 C. Kittel, *Introduction to Solid State Physics*, Wiley, 2004.
- 63 J. Li, H. K. Mao, Y. Fei, E. Gregoryanz, M. Erements and C. S. Zha, *Phys. Chem. Miner.*, 2002, **29**, 166–169.
- 64 B.-J. Lee and J.-W. Jang, *Acta Mater.*, 2007, **55**, 6779–6788.
- 65 D. C. Sorescu, *Catal. Today*, 2005, **105**, 44–65.
- 66 P. Söderlind, L. H. Yang, J. A. Moriarty and J. M. Wills, *Phys. Rev. B*, 2000, **61**, 2579.
- 67 C. Domain and C. S. Becquart, *Phys. Rev. B*, 2001, **65**, 024103.
- 68 P. A. Korzhavyi, I. A. Abrikosov, B. Johansson, A. V. Ruban and H. L. Skriver, *Phys. Rev. B*, 1999, **59**, 11693.
- 69 E. Hayward and C.-C. Fu, *Phys. Rev. B*, 2013, **87**, 174103.
- 70 S. M. Myers, P. M. Richards, W. R. Wampler and F. Besenbacher, *J. Nucl. Mater.*, 1989, **165**, 9–64.
- 71 Y. K. Shin, H. Kwak, C. Zou, A. V. Vasenkov and A. C. T. van Duin, *J. Phys. Chem. A*, 2012, **116**, 12163–12174.
- 72 W. C. Chiou Jr. and E. A. Carter, *Surf. Sci.*, 2003, **530**, 88–100.
- 73 G. Kresse and J. Hafner, *Phys. Rev. B*, 1993, **48**, 13115.
- 74 G. Kresse and J. Furthmüller, *Phys. Rev. B*, 1996, **54**, 11169.
- 75 P. E. Blöchl, *Phys. Rev. B*, 1994, **50**, 17953.
- 76 A. C. van Duin, B. V. Merinov, S. S. Han, C. O. Dorso and W. A. Goddard III, *J. Phys. Chem. A*, 2008, **112**, 11414–11422.
- 77 K. Kiuchi and R. B. McLellan, *Acta Metall.*, 1983, **31**, 961–984.
- 78 H. Z. Fang, S. L. Shang, Y. Wang, Z. K. Liu, D. Alfonso, D. E. Alman, Y. K. Shin, C. Y. Zou, A. C. T. van Duin, Y. K. Lei and G. F. Wang, *J. Appl. Phys.*, 2014, **115**, 043501.
- 79 L. K. Mansur, *J. Nucl. Mater.*, 1994, **216**, 97–123.
- 80 G. R. Odette, M. J. Alinger and B. D. Wirth, *Annu. Rev. Mater. Res.*, 2008, **38**, 471–503.
- 81 Y. Fan, A. Kushima, S. Yip and B. Yildiz, *Phys. Rev. Lett.*, 2011, **106**, 125501.
- 82 C.-C. Fu, J. D. Torre, F. Willaime, J.-L. Bocquet and A. Barbu, *Nat. Mater.*, 2005, **4**, 68–74.
- 83 L. K. Mansur, *Kinet. Nonhomogeneous Process. Pract. Introd. Chem. Biol. Phys. Mater. Sci. GR Freeman Ed Wiley N. Y.*, 1987, 377–463.
- 84 T. P. Senftle, M. J. Janik and A. C. T. van Duin, *J. Phys. Chem. C*, 2014, **118**, 4967–4981.
- 85 M. Eldrup and B. N. Singh, *J. Nucl. Mater.*, 2003, **323**, 346–353.
- 86 M. Iino, *Metall. Trans. A*, 1978, **9**, 1581–1590.
- 87 A. Arya and E. A. Carter, *J. Chem. Phys.*, 2003, **118**, 8982–8996.
- 88 D. S. Zhou and G. J. Shiflet, *Metall. Trans. A*, 2013, **23**, 1259–1269.
- 89 M. W. Finnis, *J. Phys. Condens. Matter*, 1996, **8**, 5811.
- 90 X.-G. Wang, J. R. Smith and M. Scheffler, *Phys. Rev. B*, 2002, **66**, 073411.
- 91 H. Hanada, T. Otsuka, H. Nakashima, S. Sasaki, M. Hayakawa and M. Sugisaki, *Scr. Mater.*, 2005, **53**, 1279–1284.

## ARTICLE

# Interaction of Hydrogen with the Iron and Iron Carbide Interfaces: A ReaxFF Molecular Dynamics Study<sup>†</sup>

Cite this: DOI: 10.1039/x0xx00000x

Md Mahbul Islam,<sup>a,b</sup> Chenyu Zou,<sup>b</sup> Adri C. T. van Duin,<sup>b,c</sup> and Sumathy Raman<sup>\*d</sup>Received 00th January 2012,  
Accepted 00th January 2012

DOI: 10.1039/x0xx00000x

www.rsc.org/

Hydrogen embrittlement (HE) is a well-known material phenomenon that causes significant loss in the mechanical strength of structural iron and often leads to catastrophic failures. In order to provide a detailed atomistic description of HE we have used a reactive bond order potential to describe adequately the diffusion of hydrogen as well as its chemical interaction with other hydrogen atoms, defects, and the host metal. The currently published ReaxFF force field for Fe/C/H systems was originally developed to describe Fischer-Tropsch (FT) catalysis [C. Zou, A. C. T. van Duin and D. C. Sorescu, *Top. Catal.*, 2012, 55, 391–401] and had been especially trained for surface formation energies, binding energies of small hydrocarbon radicals on different surfaces of iron and the barrier heights of surface reactions. We merged this force field with the latest ReaxFF carbon parameters [S. Goverapet Srinivasan, A. C. T. van Duin and P. Ganesh, *J. Phys. Chem. A*, 2015, 119, 1089–5639] and used the same training data set to refit the Fe/C interaction parameters. The present work is focused on evaluating the applicability of this reactive force field to describe material characteristics, and to study the role of defects and impurities in the bulk and at the precipitator interfaces. We study the interactions of hydrogen with pure and defective  $\alpha$ -iron (ferrite), Fe<sub>3</sub>C (cementite), and ferrite-cementite interfaces with a vacancy cluster. We also investigate the growth of nano voids in  $\alpha$ -iron using a grand canonical Monte Carlo (GCMC) scheme. The calculated hydrogen diffusion coefficients for both ferrite and cementite phases predict a decrease in the work of separation with increasing hydrogen concentration at a ferrite-cementite interface, suggesting a hydrogen-induced decohesion behavior. Hydrogen accumulation at the interface was observed during molecular dynamics (MD) simulations, which is consistent with experimental findings. These results demonstrate the ability of the ReaxFF potential to elucidate various aspects of hydrogen embrittlement in  $\alpha$ -iron and hydrogen interaction at a more complex metal/metal carbide interface.

## 1. Introduction

Hydrogen is well known for its deleterious effect on mechanical properties of metals and alloys.<sup>1–4</sup> In metallic systems, such as carbon steels, the presence of hydrogen often embrittles the material, a phenomenon known as hydrogen embrittlement (HE). The structural iron used in refinery industries and in oil and gas pipelines are particularly susceptible to HE due to their exposure to the hydrogen-rich environment. HE has received an enormous amount of research attention over the last few decades.<sup>5–7</sup> Many mechanisms have been proposed to explain HE. The inclusion of a few parts per million (ppm) of hydrogen in carbon steels can dramatically reduce fracture stress, strain, and ductility while also enhances brittleness, these often leads to disastrous brittle failure without plastic strain.<sup>8,9</sup> A hydrogen-induced delayed fracture mechanism has also been proposed, wherein the presence of hydrogen is known to initiate a crack in the material at an applied load that is lower than the yield stress of the material.<sup>10</sup> Beachem<sup>11</sup> suggests that subcritical crack growth in the material due to localized plastic deformation is prompted by the interaction of hydrogen with dislocations. The hydrogen-enhanced localized plasticity (HELP) theory predicts material failure due to the hydrogen-induced high mobility of dislocations, resulting in an increased local plasticity

and agglomeration of dislocations, leading to a plastic failure.<sup>12</sup> The mechanism of hydrogen enhanced decohesion (HEDE) has also been discussed widely as a mechanism for embrittlement in structural iron.<sup>13,14</sup> HEDE postulates that the accumulation of hydrogen in the lattice sites weakens the bonding strength between atoms of the host metal and reduces the material strength. The Griffith criteria suggests that the presence of hydrogen lowers surface energy and accelerates cleavage-like failures along the crystal planes of the material. HEDE damage occurs in crack tips and interfaces, where the presence of hydrogen lowers atomic cohesive strength and initiates interfacial debonding; consequently, cracks propagate at a lower applied tensile loading.<sup>15</sup> In general, these proposed models explain certain aspects of HE; however, a comprehensive mechanism has not been derived so far.<sup>6,16–18</sup>

Hydrogen inclusion in a material may happen during manufacturing, processing, or when the material is exposed to a hydrogen rich environment during its service life. Hydrogen traps at various lattice defects — dislocations, microvoids, grain boundaries, and precipitator interfaces — result in an increased amount of dissolved hydrogen in carbon steels. This is due to the fact that the trapping sites are generally lower in energy than the regular lattice sites.<sup>19,20</sup> Once introduced in the bulk iron, hydrogen diffuses quickly through

the tetrahedral interstitial sites until it finds a trap or a surface such as a vacancy or an interface.<sup>15</sup> Therefore, the processes of hydrogen trapping and diffusion in metallic materials are considered to be important elementary steps for developing an improved understanding of the mechanisms of HE.

Furthermore, numerous reports suggest that the inclusion of various non-metallic phases in high-strength carbon steel plays a significant role in the process of HE and in determining mechanical properties of the materials. Non-metallic precipitators may act as a strong trapping site and a retardant for the diffusing hydrogen atoms.<sup>10</sup> Hydrogen trapping at an interface could impact the decohesion of the host metal and initiate a crack.<sup>6</sup> Chan et al.<sup>21</sup> reported that the ferrite-cementite interfaces are dominant trapping sites for hydrogens owing to a relatively lower interfacial energy. Ramunni et al.<sup>22</sup> described the cementite phase as a major trapping site for hydrogen. Lee and co-workers<sup>23,24</sup> studied hydrogen trapping by TiC particles and the activation energy for the trapping of hydrogen. Other researchers<sup>25,26</sup> suggest that the presence of inclusions introduces voids, increases hydrogen concentration in the voids, and supports the growth of voids under the application of tensile loading. Consequently, crack initiation and propagation happens along the inclusion-metal interfaces.

Despite a great deal of research effort to explain the interaction of hydrogen with structural steel, a detailed understanding at an atomistic level has not been fully developed. The high mobility and low solubility of hydrogen in  $\alpha$ -iron impedes experimental techniques to offer a detailed characterization of the hydrogen interaction.<sup>27</sup> In this regard, atomistic simulations can effectively assist to probe different proposed hypotheses to gain insight into the underlying mechanism of HE on a length and time scale that is not accessible in experiments. Both the *ab-initio* and the classical molecular dynamics simulations have been employed in studying the iron-hydrogen systems. The static Density Functional Theory (DFT)-based *ab-initio* calculations focus primarily on ground-state energies of elementary steps to derive an understanding of the reaction paths as well as barriers of the reaction steps for hydrogen interactions with  $\alpha$ -iron while the classical simulations based on non-reactive force field focused on predicting the mechanical properties and the impact of hydrogen. Many atomistic simulation studies on iron-hydrogen systems are available in the literature, such as diffusion of hydrogen through bulk iron,<sup>28–31</sup> the trapping of hydrogen at vacancies,<sup>32–34</sup> and hydrogen accumulation at the crack tips.<sup>2</sup>

Moreover, the literature shows that efforts were made to implement a kinetic Monte Carlo (KMC) scheme to simulate the time evolution of a complex phenomenon like HE from the list of elementary steps together with their rates being identified using the high level DFT calculations.<sup>35,36</sup> Such a scheme is attractive and advantageous as it provides a more fundamental insight if the list of transitions in the transition table is complete. The latter is more challenging, especially when it involves surfaces and interfaces. In addition, owing to the complexity of the interfacial structures, no *ab-initio* or classical molecular dynamics studies have been conducted on hydrogen interaction with a ferrite-cementite interface. In this regard, the ReaxFF method is an attractive option as it is computationally less demanding compared to the *ab-initio* MD and/or the efforts needed upfront to explore the detailed DFT based potential energy surface for a KMC simulation. In addition, ReaxFF has demonstrated its ability to describe complex interfaces in a number of studies.<sup>37–39</sup>

In this study, we employed the ReaxFF reactive force field method to investigate vacancy-hydrogen interaction in a bulk  $\alpha$ -iron phase, the interaction of hydrogen at the ferrite-cementite interfaces, and void nucleation and growth of nanovoids in the  $\alpha$ -iron. In addition, this work also explores the applicability of the Fe/C/H ReaxFF force field—which was originally developed and recently updated against the training set to describe elementary reactions in Fischer-Tropsch catalysis<sup>40</sup>—to investigate the chemistry of hydrogen interaction with the bulk iron and at the interfaces of ferrite-cementite phases.

The next section briefly describes the ReaxFF formalism and is followed by force field validation results for pure and defective iron, as well as for the  $\alpha$ -iron and Fe<sub>3</sub>C surfaces. Subsequent sections highlight the molecular dynamics simulation results on the diffusion of hydrogen in bulk  $\alpha$ -iron and Fe<sub>3</sub>C phases, growth of nanovoids, and hydrogen interaction with  $\alpha$ -iron in presence of a nanovoid and at interfaces

## 2. ReaxFF Background and Force Field Description

ReaxFF is a general bond order<sup>41,42</sup> (BO) based empirical force field method which allows bond breaking and formation in a dynamic simulation. The general form of the ReaxFF energy is shown below:

$$E_{\text{system}} = E_{\text{bond}} + E_{\text{over}} + E_{\text{under}} + E_{\text{lp}} + E_{\text{val}} + E_{\text{tor}} + E_{\text{vdWaals}} + E_{\text{Coulomb}}$$

It includes, respectively, partial energy contributions from the bond, over-coordination penalty and under-coordination stability, lone pair, valence, and torsion, non-bonded interactions van der Waals, and Coulomb energies.

ReaxFF uses the concept of bond orders to determine the bonded interactions among all atoms in a system. BO is a continuous function of distance between bonded atoms and accounts for contributions from sigma, pi, and double-pi bonds using the following expression.

$$\begin{aligned} BO'_{ij} &= BO_{ij}^{\sigma} + BO_{ij}^{\pi} + BO_{ij}^{\pi\pi} \\ &= \exp \left[ p_{bo1} \cdot \left( \frac{r_{ij}}{r_o^{\sigma}} \right)^{p_{bo2}} \right] \\ &\quad + \exp \left[ p_{bo3} \cdot \left( \frac{r_{ij}}{r_o^{\pi}} \right)^{p_{bo4}} \right] \\ &\quad + \exp \left[ p_{bo5} \cdot \left( \frac{r_{ij}}{r_o^{\pi\pi}} \right)^{p_{bo6}} \right] \end{aligned}$$

where  $BO_{ij}^{\sigma}$ ,  $BO_{ij}^{\pi}$ , and  $BO_{ij}^{\pi\pi}$  are the partial contributions of  $\sigma$ ,  $\pi$ - and double  $\pi$ -bonds between atoms  $i$  and  $j$ ,  $r_{ij}$  is the distance between  $i$  and  $j$ ,  $r_o^{\sigma}$ ,  $r_o^{\pi}$ , and  $r_o^{\pi\pi}$  are the bond radii of  $\sigma$ ,  $\pi$ - and double  $\pi$ -bonds, respectively, and  $p_{bo}$  terms are empirical parameters fit to either experimental or quantum data.

All of the connectivity-dependent interactions, i.e. the valence and torsion energy, are contingent on BO, therefore, as bond breaks their energy contribution also diminishes. Bonded and non-bonded interaction energies are calculated independently. Non-bonded interactions, i.e. the van der Waals and Coulomb, are calculated between every pair of atoms, regardless of their connectivity. Excessive repulsion at short distances is circumvented by adding a

shielding parameter in non-bonded energy expressions and a 7<sup>th</sup> order taper function is used to eliminate any energy discontinuity.<sup>43,44</sup> The combination of covalent and Coulomb interactions enables ReaxFF to describe a wide range of systems, including covalent,<sup>45,46</sup> metallic,<sup>47</sup> metal hydride,<sup>48</sup> and carbide<sup>40</sup> systems. ReaxFF uses a geometry-dependent charge calculation scheme, the Electronegativity Equalization Method (EEM)<sup>49</sup> for charge calculation. ReaxFF method have been widely used to investigate a wide range of applications in materials,<sup>50-53</sup> catalysis<sup>54</sup>, and other chemical systems.<sup>55,56</sup> For a more detailed description of the ReaxFF method, see van Duin et al.,<sup>46</sup> Chenoweth et al.,<sup>45</sup> and Russo Jr et al..<sup>57</sup>

The original Fe/C/H ReaxFF force field<sup>40</sup> parameters were developed through extensive training against high-level quantum data for describing the equation of state of  $\alpha$ - and  $\gamma$ -phases of iron, and Fe<sub>3</sub>C, hydrogen interaction at different surfaces of  $\alpha$ -iron, surface formation energies of  $\alpha$ -iron and Fe<sub>5</sub>C<sub>2</sub>, binding energies of small hydrocarbon radicals on different surfaces of iron, and hydrogen dissolution in bulk iron at different concentrations. A detailed description of the force field development can be found in Ref.[40]. For this work, we retained the Fe/Fe and Fe/H parameters from the FT catalysis force field<sup>40</sup> and merged these with the recently developed ReaxFF carbon parameters.<sup>58</sup> Next, we performed refitting for Fe-C bond and 6 angle parameters, viz., Fe-C-Fe, H-C-Fe, C-Fe-C, C-Fe-H, C-H-Fe and Fe-C-H to restore the force field error to the same level as the original Fe/C/H force field.<sup>40</sup> This refitting was performed using the same training set data as used in ref.[1]. Key force field parameters are presented in Table I-IV. Detailed force field parameters are given in the supporting information.

One of the value added claims for any force field is transferability and this work demonstrates that the force field developed to address Fischer-Tropsch catalysis can be used to describe vacancies, vacancy migration, vacancy void formation and vacancy-hydrogen cluster formation in  $\alpha$ -iron and hydrogen interactions with the ferrite-cementite interfaces. While, the force field used in this study has been developed based on the two previously published work, none of those works evaluated the applicability of the force field for vacancy, hydrogen-vacancy interactions, interface energies, work of separation or diffusion of hydrogen.

Table I. Fe/C/H selected atom parameters

	$r_0$ (Å)	$\eta$ (eV)	$\chi$ (eV)	$\gamma$ (Å)	$P_{ov/un}$
Fe	1.9306	8.6241	1.7785	0.4744	-16.0573
C	1.3674	7.0000	4.8446	0.8485	-4.1021
H	0.8930	9.6093	3.7248	0.8203	-19.4571

For a definition of the parameters, see reference [46]

Table II. Fe/C/H selected bond parameters

	$D_e^\sigma$ (kcal/mol)	$P_{be,1}$	$P_{be,2}$	$P_{bo,1}$	$P_{bo,2}$	$P_{kov}$
Fe-Fe	44.2147	0.2236	0.4922	-0.0552	6.7583	0.2849
C-Fe	103.5536	0.8440	0.7522	-0.1509	4.0000	0.0100
H-Fe	78.2669	0.4668	0.5673	-0.1543	5.4965	0.1766

For a definition of the parameters, see reference [46]

Table III: Fe/C/H selected off diagonal bond parameters

	$D_{ij}$ (kcal/mol)	$R_{vdw}$ (Å)	$\alpha$	$r_0^\sigma$ (Å)
Fe-C	0.3999	1.4558	11.0036	1.3918
Fe-H	0.0200	1.9451	10.8595	1.4157
C-H	0.1200	1.3861	9.8561	1.1254

For a definition of the parameters, see reference [46]

Table IV. Fe/C/H selected angle parameters

	$\theta_0$ (degree)	$k_a$ (kcal/mol)	$k_b$ (1/rad) <sup>2</sup>	$P_{v,1}$	$P_{v,2}$
Fe-C-Fe	29.2204	18.5882	4.2644	0.0832	1.1249
H-C-Fe	0.3090	16.1111	1.4583	0.0100	1.4801
C-Fe-C	0.0100	39.5131	4.3816	0.5791	3.7111
C-Fe-H	48.0872	0.3787	0.0108	0.3648	1.5939
C-H-Fe	0.0100	2.8313	2.3314	2.7564	2.7554
Fe-C-H	0.3090	16.1111	1.4583	0.0100	1.4801

For a definition of the parameters, see reference [46]

### 3. Force Field Validation

In the present study, we performed a set of calculations to evaluate the capability of the Fe/C/H force field. Our objective was to investigate the interactions of hydrogen with the pure and defective bulk  $\alpha$ -iron, as well as at the ferrite-cementite interfaces. For this purpose, we evaluated our force field performance in a series of relevant cases and compared our calculated values with the data available in literature either from experiments or from high-level *ab-initio* computations.

#### 3.1 Bulk Properties of $\alpha$ -Iron and Fe<sub>3</sub>C

The bulk mechanical properties of  $\alpha$ -iron and Fe<sub>3</sub>C phases were investigated. In order to calculate the equilibrium lattice constants and the bulk moduli of both  $\alpha$ -iron and Fe<sub>3</sub>C, we performed simulations to obtain the energy-volume relationships. In this simulation, we applied both compression and expansion with respect to the equilibrium volume and recorded the corresponding energies. The equations of states as calculated from ReaxFF simulations and the corresponding DFT data for  $\alpha$ -iron<sup>59</sup> and Fe<sub>3</sub>C<sup>60</sup> are shown in Fig.1. The minimum of the energy-volume curve provides the equilibrium lattice constant and bulk modulus were calculated by fitting the data using Murnaghan equation of state. ReaxFF predicted equilibrium lattice constants of  $\alpha$ -iron and Fe<sub>3</sub>C are respectively:  $a=2.85\text{Å}$ , and  $a=5.09$ ,  $b=6.74$ ,  $c=4.53\text{Å}$ , which are in good agreement with the experimental data.<sup>61,62</sup> The bulk modulus values of the  $\alpha$ -iron and Fe<sub>3</sub>C phase as calculated from the Murnaghan equation of state are: 148 and 136 GPa, and they are in accordance with the reported literature value of  $168^{62}$  and  $174\pm 6\text{ GPa}$ ,<sup>63</sup> respectively.

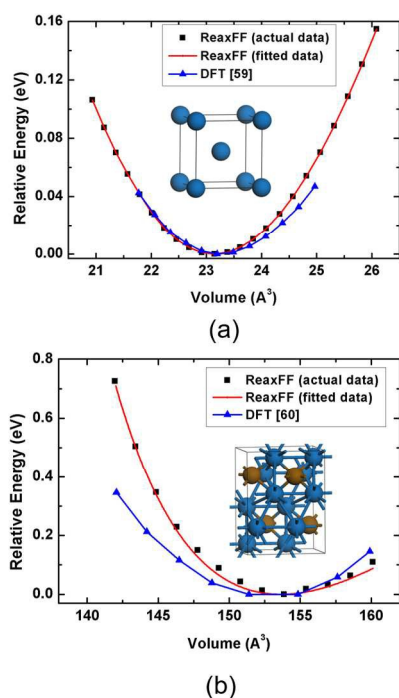


Fig. 1. Equation of states of (a)  $\alpha$ -iron and (b)  $\text{Fe}_3\text{C}$  phases as calculated using ReaxFF method and corresponding DFT values. Color scheme: carbon (ochre), and Iron (blue)

### 3.2 Hydrogen Binding and Diffusion in Bulk Iron

For the computation of hydrogen binding energies in bulk  $\alpha$ -iron, we considered an  $8 \times 8 \times 8$  supercell of the  $\alpha$ -iron. The bcc lattice has two high symmetry interstitial sites, namely, octahedral (O-site) and tetrahedral (T-site). It is well known that hydrogen dissolution in the bulk-iron is endothermic. Our calculated hydrogen dissolution energies are, respectively, 0.40 and 0.64 eV corresponding to the tetrahedral and octahedral sites. These values are in agreement with the data reported by other authors, such as 0.33-0.35 eV for the T-site,<sup>64</sup> and 0.43-0.55 eV for the

O-site.<sup>31,65</sup> Hydrogen prefers to occupy the T-sites, and it is reported in the literature as the ground state for interstitial hydrogen,<sup>34</sup> while O-sites are not preferred due to the requirement of a larger lattice expansion to accommodate the hydrogen.<sup>31</sup> However, at elevated temperatures, hydrogen tends to occupy the octahedral sites. Jiang et al.<sup>31</sup> reported from their first principles calculations that the hydrogen dissolution energies at the T-sites are quite insensitive to the hydrogen concentration in the bulk-iron due to the absence of strong H-H interactions. Therefore, the presence of multiple hydrogens does not significantly affect the per hydrogen binding energy in the bulk-iron. Hydrogen diffusion barriers are also calculated for interstitial hopping. Two predominant diffusion pathways, such as T-T and T-O-T, are reported in literature. ReaxFF predicted diffusion barriers for T-T and T-O-T are, respectively, 0.032 and 0.3 eV, which are qualitatively consistent with the DFT calculated values of, respectively, 0.082 eV<sup>31</sup> and 0.19 eV.<sup>65</sup>

### 3.3 Vacancy Formation and Interaction with Hydrogen

A vacancy is a configuration in which an atom is missing from a regular lattice site. Vacancy plays an important role in Fe-H interactions. We calculated a monovacancy formation energy as 2.5 eV, which is in agreement with the results from other DFT studies (1.95-2.76 eV)<sup>66-68</sup> and close to the reported experimental range of 1.6-2.1 eV.<sup>34,69</sup> The monovacancy formation energy was calculated using supercells of different sizes to eliminate the size effect. The vacancy migration barriers to the first and second nearest neighbors as calculated from the ReaxFF are, respectively, 0.83 eV and 2.95 eV, while the reported values in the literature are, respectively, 0.69 and 2.50 eV.<sup>69</sup> ReaxFF slightly overpredicts the vacancy migration barriers. It was observed that the presence of hydrogen in a lattice reduces vacancy formation energies.<sup>69</sup> The monovacancy formation energy in the vicinity of  $n$  hydrogen cluster is calculated using the following formula:

$$E_V^f = E(H_nV) - \frac{N-1}{N}E_0 - n[E(H_T) - E_0]$$

where,  $E(H_nV)$  is the energy with a vacancy-hydrogen cluster,  $N$  is the number of iron atoms in the perfect lattice with energy  $E_0$ ,  $n$  is the number of hydrogens, and  $E_T$  is the energy with a hydrogen atom at the T-site.

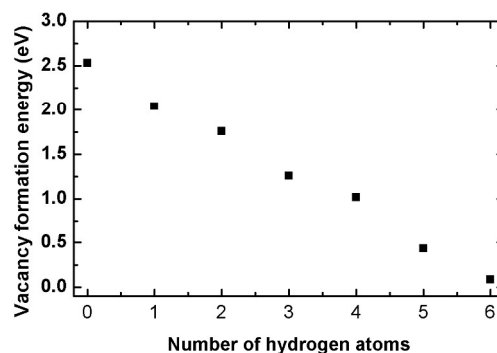


Fig. 2. Vacancy formation energies in presence of hydrogen clusters of various sizes in the vicinity of a monovacancy

ReaxFF predicts a systematic reduction in vacancy formation energies with the increasing number of hydrogens in the cluster that is consistent with previous DFT result.<sup>69</sup> Vacancy formation energy reduces to 0.08 eV in the presence of a cluster of six hydrogens around a monovacancy. ReaxFF predicted results of the vacancy formation energies in the presence of hydrogen clusters of various sizes are shown in Fig. 2.

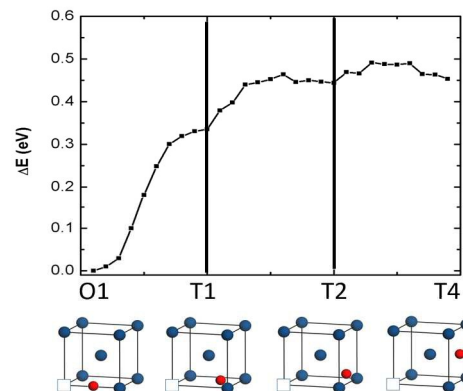


Fig. 3. The barriers to diffusion of a hydrogen-vacancy pair in bulk  $\alpha$ -iron. The hydrogen-vacancy pair configurations are shown

schematically. White square and red sphere represent vacancy and hydrogen, respectively.

In a bcc-lattice, there are six possible sites around a monovacancy for trapping hydrogens. These sites are located near the octahedral sites of a bcc-lattice adjacent to the monovacancy as stated by Myers et al.<sup>70</sup> Vacancies form a strong trap for the hydrogen diffusing through the bulk. The incremental hydrogen trap energy in a monovacancy is calculated as:

$$E_{\text{trap}}(m,n)=[E(m,n-1)-E(0,m)]-[E(m,n)+E(0,0)]$$

where  $n$  and  $m$  are the number of hydrogens and vacancies, respectively. ReaxFF predicted hydrogen binding energies in a monovacancy site are tabulated in Table V. One can see that the ReaxFF results are in reasonable agreement with the available literature data.<sup>34</sup>

Table V. Hydrogen binding in a monovacancy site of  $\alpha$ -iron. For comparison results are shown from the previous DFT studies performed by Tateyama et al.<sup>36</sup>

Nr. of H	ReaxFF (eV)	Ref. [34] (eV)
1	0.50	0.55
2	0.45	0.51
3	0.50	0.40
4	0.32	0.27
5	0.24	0.33
6	-0.30	-0.019

We also calculated hydrogen diffusion barriers in the presence of a monovacancy. The energy barriers are calculated for hydrogen diffusion from one octahedral site to three other tetrahedral sites. The schematics of diffusion pathways are shown in Fig. 3 along with the corresponding relative energies. Comparison of the results with the DFT data from Hayward et al.<sup>69</sup> suggests a good agreement for the calculated energy barriers. All of these calculations establish the quality of the force field in predicting the vacancy-hydrogen interactions in  $\alpha$ -iron.

### 3.4 Surface Formation Energies of $\alpha$ -iron and Fe<sub>3</sub>C

We computed surface formation energies of both  $\alpha$ -iron and Fe<sub>3</sub>C and compared them with literature values. Three different  $\alpha$ -iron surfaces were considered in this study, namely, (110), (100), and (111). Surface formation energies were checked for the convergence with the number of layers, and in these computations, eight layers were found to be sufficient for the convergence in the energy within 0.01 Jm<sup>-2</sup>. Surface formation energies are calculated using the following relation:

$$\Delta E_s = \frac{1}{2A_s} (E_{\text{slab}} - nE_{\text{bulk}})$$

where,  $A_s$  is the surface area and  $E_{\text{slab}}$  and  $E_{\text{bulk}}$  are the energies of the slab and the bulk iron, respectively. ReaxFF predicted (110), (100), (111) surface formation energies are 2.15, 2.29, 2.59 Jm<sup>-2</sup>, respectively, while at the QM level, the values correspond to 2.29, 2.30, 2.59 Jm<sup>-2</sup>.<sup>71</sup> It can be seen that ReaxFF accurately reproduces the QM surface formation energies and the relative stability of each of the surfaces. ReaxFF predicted the (110) surface of  $\alpha$ -iron as the most stable surface and this is in agreement with the findings using high level quantum calculations.<sup>71</sup>

We considered three different Fe<sub>3</sub>C surfaces—(001), (010), and (100)—for surface formation energy calculations. Surface formation energies predicted by the ReaxFF for (001), (010), and (100) are, respectively, 2.06, 1.98, and 2.52 Jm<sup>-2</sup>, in close proximity with the corresponding QM data<sup>72</sup> of 2.05, 2.26, and 2.47 Jm<sup>-2</sup>, respectively. However, the ReaxFF prediction of the lowest energy surface is in contradiction with the results from quantum computations.<sup>72</sup> ReaxFF calculations show nearly an equal stability for both the (001) and (010) surfaces, while the result from quantum computations directs the (001) surface as the lowest energy surface.

### 3.5 H-binding in Fe<sub>3</sub>C Surfaces

We carried out the DFT calculations for the binding energy of hydrogen at different Fe<sub>3</sub>C surfaces. The Vienna ab initio simulation package (VASP) was employed to solve Kohn-Sham equations with a plane-wave basis set.<sup>73,74</sup> We used Blöchl's all-electron frozen core projector augmented wave (PAW) method<sup>75</sup> to represent core electron regions with valence configurations of 3d<sup>7</sup> 4s<sup>1</sup> for Fe atoms and 1s<sup>1</sup> for H atoms and the generalized gradient approximation (GGA) of PBE was used to treat the exchange-correlation functional. A 15Å vacuum was introduced in the surface normal direction while periodic boundary condition was used in the other two directions. The atomic force convergence criterion for the structural optimizations was set as 0.05 eV Å<sup>-1</sup>. The Monkhorst-Pack (MP) Brillouin zone sampling method was used with a 9x11x10 k-point spacing and an energy cutoff of 450eV. In these calculations, zero point energy for the hydrogen was not considered. Our calculated DFT energies for the binding of a hydrogen atom at the (100), (010), and (001) surfaces are, respectively, -0.65, -0.60, and -0.46 eV, while the ReaxFF predicted energies are, respectively, -0.56, -0.67, and -0.57 eV. ReaxFF qualitatively reproduces DFT energies for the binding of hydrogen at the Fe<sub>3</sub>C surfaces considered in this study. Hydrogen binds at the three-folded sites of (100) and (010) surfaces, while for (001) surface hydrogen binds at a bridge site between two iron atoms. Three-fold binding sites are more stable than the bridge sites, and this is evident from the DFT energies as well. However, the ReaxFF predictions for the binding energies at the (100) and (010) surfaces are quite similar. In this study, it was important for the ReaxFF to capture the qualitative trend for hydrogen binding with the surfaces to describe the hydrogen interactions at the interfaces. For hydrogen binding data at the  $\alpha$ -iron surfaces, readers are referred to the ref. [40].

## 4. Results and Discussion

### 4.1 Hydrogen Diffusion Coefficients in Bulk $\alpha$ -iron and Fe<sub>3</sub>C

To calculate the diffusion coefficient of hydrogen in the bulk  $\alpha$ -iron, we performed NVT-MD simulations at various temperatures, such as, 300K, 400K, 500K, and 600K, with a temperature damping constant and a MD time step of 500 and 0.25 femtoseconds, respectively. Hydrogen atoms were randomly loaded in the bcc-lattice of iron at varying concentrations. Various system sizes and hydrogen concentrations were considered for this study. Supercell sizes of 8x8x8, 10x10x10, 14x14x14, and 18x18 x18 unit cells were chosen. The range of hydrogen concentration from 10<sup>-4</sup> to 10<sup>-2</sup> (hydrogen concentration is defined as the ratio of number of hydrogen to the number of iron atoms) was investigated. A

periodic boundary condition was employed in all three directions. A conjugate gradient energy minimization scheme was used to perform the structural relaxation. During the MD simulations, trajectories were saved at every 0.125 picosecond. Diffusion coefficients were computed using the mean square displacement (MSD) of hydrogen atoms that was determined from the unfolded atomic coordinates after the system achieved equilibrium at the simulation temperature. MSDs and diffusion coefficients (DCs) were calculated using the Einstein's relation:

$$MSD = \langle |r(t) - r(0)|^2 \rangle$$

$$D = \frac{1}{6} \lim_{\Delta t \rightarrow \infty} \frac{MSD(t + \Delta t) - MSD(t)}{\Delta t}$$

where  $r$  is the position of the particle,  $t$  is the time, and  $D$  is the diffusion coefficient.

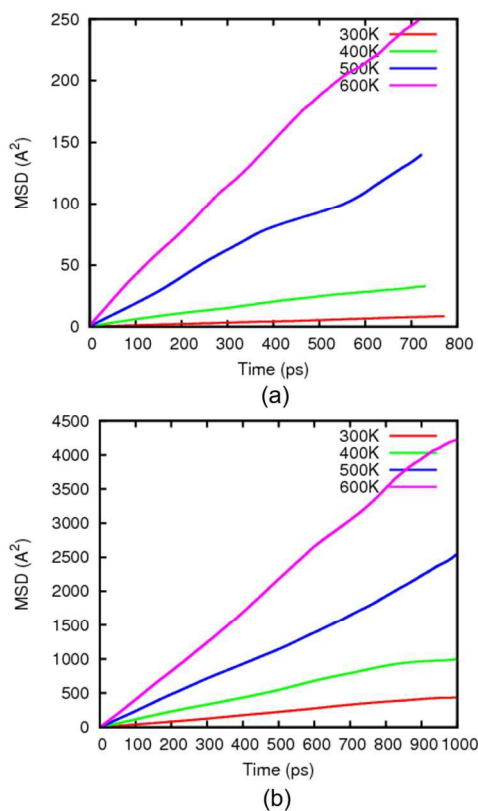


Fig. 4. MSD vs. time plot at various temperatures for diffusion of hydrogen in (a)  $\alpha$ -iron (b)  $Fe_3C$  phase

The apparent DC were calculated using the following Arrhenius equation:<sup>76</sup>

$$D(T) = D_0 \exp\left(-\frac{E_a}{kT}\right)$$

where  $D_0$  is the pre-exponential factor,  $E_a$  is the activation energy,  $k$  is the Boltzmann constant, and  $T$  is the temperature. The activation energy and the pre-exponential factors are independent of temperature and were computed using an exponential regression analysis of a  $D$  vs.  $1/T$  plot. Figure 4(a) shows MSD vs. time plot for the hydrogen concentration of  $10^{-2}$  in the bulk  $\alpha$ -iron. The statistical average of the diffusion coefficient results derived from ten different simulations at four

different temperatures is shown in Fig. 5 with error bars. The mean hydrogen diffusion coefficient at 300K is calculated as  $7.1 \times 10^{-10} \text{ m}^2 \text{ s}^{-1}$ . ReaxFF underestimates the experimental diffusion coefficient by about 50% in comparison with the experimental data in [77]. The magnitude of this deviation can be attributed to the relatively higher hydrogen concentration considered in this study as well to the time-scales used in these computations. Pre-exponential factors and activation barriers are calculated using least-square regression analysis. We represent the diffusion coefficient as a function of temperature with the following expression:  $D(T) = 5 \times 10^{-8} \exp(-1318/T) \text{ m}^2 \text{ s}^{-1}$ . The activation barrier for hydrogen diffusion is calculated as 0.11 eV.

The activation barrier calculated from the MSD plot is relatively higher than the barrier calculated from the static calculation for the minimum energy diffusion pathway (T-T jump), which implies—H diffusion mechanism cannot be solely attributed to the T-T jump. Due to the temperature effect, T-O-T jump also has a finite probability. At a higher temperature, higher entropy also facilitates T-O-T jump. In addition, hydrogen-hydrogen interaction affects hydrogen diffusion barrier in our dynamic simulations.<sup>78</sup> The hydrogen diffusion mechanism in pure  $\alpha$ -iron can be attributed to the interstitial diffusion only—predominantly through the T-T site, however, T-O-T diffusion was also observed during the simulation.

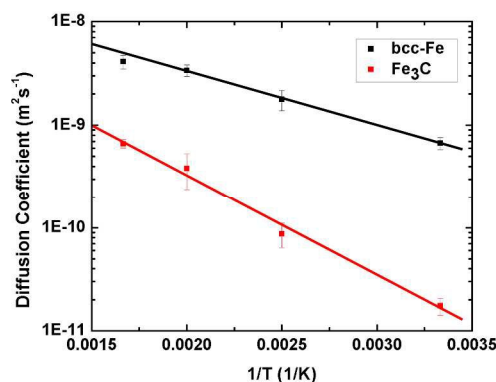


Fig. 5. Diffusion coefficient of hydrogen in the  $\alpha$ -iron and  $Fe_3C$  phases as a function of temperature (Y-axis is in logarithmic scale)

We also calculated the hydrogen diffusion coefficient at the  $Fe_3C$  phase following the same procedure described for the  $\alpha$ -iron simulations. The hydrogen concentration range was between  $10^{-4}$  -  $10^{-2}$  for the  $Fe_3C$ . ReaxFF predicted mean hydrogen diffusion coefficient in the  $Fe_3C$  at 300K is  $1.84 \times 10^{-11} \text{ m}^2 \text{ s}^{-1}$ , which is an order of magnitude slower than the corresponding  $\alpha$ -iron case. From the Arrhenius plot, the activation barrier and pre-exponential factor are calculated as 0.80 eV and  $3 \times 10^{-8} \text{ m}^2 \text{ s}^{-1}$ . The predicted higher activation barrier resulted in slower hydrogen diffusion in the  $Fe_3C$  phase. The calculated average diffusion coefficients at various temperature are shown in Fig. 5 along with error bars. The hydrogen diffusion coefficient as a function of temperature can be expressed as:  $D(T) = 3 \times 10^{-8} \exp(-2243/T) \text{ m}^2 \text{ s}^{-1}$ . Overall, the agreement between ReaxFF and the available literature demonstrates that the Fe/C/H potential can be used to derive hydrogen diffusion properties in the bulk  $\alpha$ -iron and  $Fe_3C$  over a range of temperatures and hydrogen concentrations.

#### 4.2 Void Nucleation and Growth in $\alpha$ -Iron

Structural materials exposed to the irradiation environment undergo changes in structure and physical properties. Irradiating particle displaces atoms from their lattice positions and creates vacancies and self-interstitial defects.<sup>79,80</sup> Iron structures of the fission and fusion reactors experience extreme radiation fields. However, the prediction of irradiation induced vacancies and their growth to form nanovoids requires a time scale (seconds to year), which is prohibitive for the conventional MD methods.<sup>81</sup> Previously, KMC<sup>82</sup> and rate theory<sup>83</sup> were used to study the void growth; however, these methods depend heavily on the reaction rates and barriers derived from atomistic simulations. In this study, we employed a relatively simplified approach—the grand canonical Monte Carlo (GCMC) scheme<sup>84</sup>—to investigate the nucleation and formation of vacancy clusters. The migration of monovacancies and their combination with other vacancies leads to the formation of a vacancy cluster. The Metropolis criteria based swap move of the GCMC scheme enabled us to investigate vacancy cluster formation. An  $\alpha$ -iron 8x8x8 supercell is used for this simulation. The initial geometry contains 50 randomly distributed monovacancies. This high vacancy concentration represents a super-abundant vacancy configuration.<sup>29</sup>

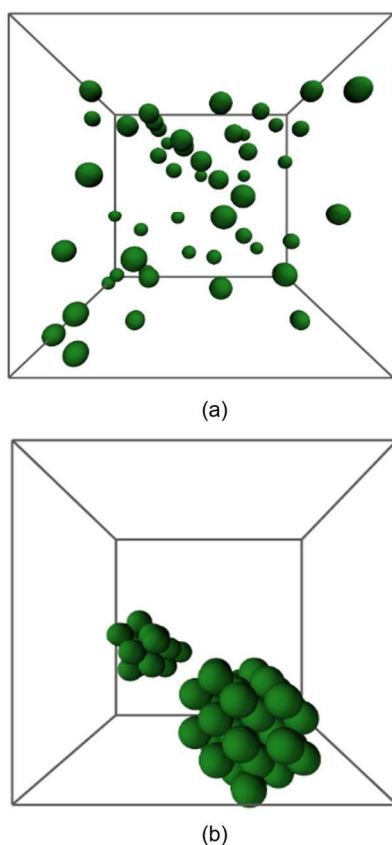


Fig. 6. Vacancy cluster formation during a GCMC simulation (a) initial vacancy distribution (b) formation of vacancy clusters (vacancies are represented as green sphere and lattice iron atoms are not shown for clarity)

A GCMC swap move was allowed only to swap a vacancy with a lattice site. The GCMC move was accepted when vacancy swapping is energetically favored. The results from this simulation are shown in Fig. 6. Large vacancy clusters comprising of 29 and 21 vacancies were observed during the GCMC move. Coalescence of the isolated

vacancies to large vacancy clusters supports the experimental evidence of nanovoids formation in irradiated iron.<sup>85</sup>

#### 4.3 Diffusion of Hydrogen in Presence of a Vacancy Cluster

Hydrogen precipitation at dislocations and voids in the  $\alpha$ -iron is a well-known phenomenon.<sup>86</sup> Strong attraction of the hydrogen towards the defect sites is a cause of increased hydrogen concentration in the voids. We performed MD simulations to study this phenomenon. We created a cubic lattice of 8x8x8 supercell of  $\alpha$ -iron, and a spherical void of 10Å diameter was introduced by removing lattice iron atoms. Twenty hydrogen atoms were randomly inserted in the simulation cell. Periodic boundary conditions were used in all three directions. After performing a structural relaxation simulation, we conducted a NVT-MD simulation at 500K with a temperature damping constant of 500fs. The simulation cell and the hydrogen trajectories from the MD simulation are shown in Fig. 7.

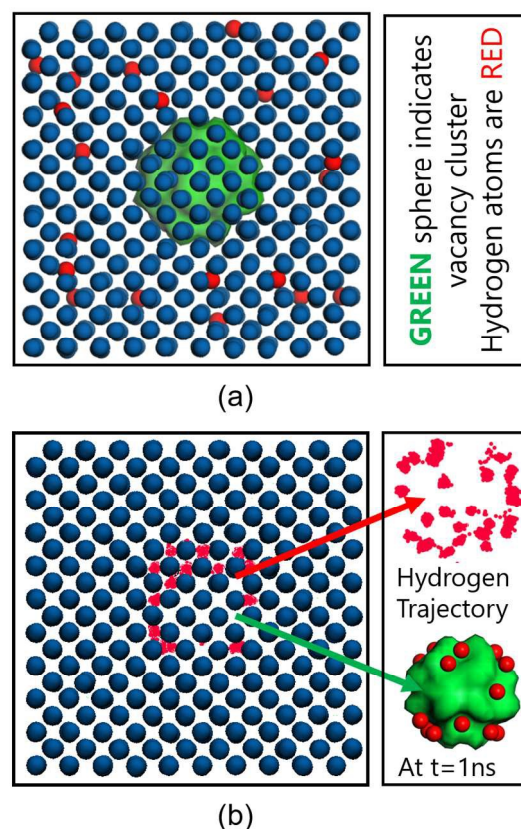


Fig. 7. Hydrogen binding at a vacancy cluster in a 500K NVT MD simulation, (a) Initial configuration, (b) Equilibrated hydrogen trajectories during this simulation. Color scheme: Iron (blue).

Hydrogen atoms diffused through the lattice, and once they arrived at the vacancy site they bonded with the inner surface. Hydrogen accumulation at the void inner surface was increased as simulation proceeded. Thus within 400ps of simulation, all the hydrogen atoms bonded at the vacancy site. This trapping of hydrogen at the vacancy cluster and an increased concentration of hydrogen at the void is consistent with the experimental observation of hydrogen induced blister formation in the pipeline steel.<sup>25</sup>

#### 4.4 Ferrite-Cementite Interface Simulations

Typically, interfaces are formed due to the presence of different precipitators in a structural iron. Commonly observed precipitators are  $\text{Fe}_3\text{C}$ ,  $\text{Fe}_2\text{C}_5$ , and  $\text{TiC}$ .<sup>24,87</sup> In this study, we considered the  $\text{Fe}_3\text{C}$  precipitator in an  $\alpha$ -iron phase and investigated the interaction of hydrogens at interfaces and also with the individual phases. Interfaces were modeled by a slab, which consists of a finite number of layers of ferrite and cementite structure. In our slab model, we considered Bagarytsky interfaces (BI) that are commonly observed in the ferrite-cementite system.<sup>88</sup> Two BIs are considered in this study, namely, C100/F1 $\bar{1}$ 0, and C010/F111, where C and F represent cementite and ferrite surfaces, respectively. Surfaces were cut from the individual bulk phases, and we constructed surface supercells of both phases so that upon interface formation, lattice mismatch is minimized. Cell dimensions of C100/F1 $\bar{1}$ 0, and C010/F111 interfaces were, respectively, 20.0 x 32.0 x 60.0 and 36.0 x 20.0 x 60.0 Å. Lattice misfit for C100/F1 $\bar{1}$ 0, and C010/F111 interfaces are, respectively, ~0.5% and ~3%. We constructed these interface geometries in the Materials studio 7. Periodic boundary conditions were employed in the y and z-directions while the x-direction was set as non-periodic (Fig 9).

In structural iron, adhesion between a precipitator and the metal interface plays a significant role in predicting their mechanical strength. Hydrogen accumulation at an interface enhances the tendency of embrittlement. It was experimentally observed that the presence of hydrogens at the interface weakens the bonding, thus leading to the propagation of decohesion-induced failure along the interfacial boundary.<sup>25</sup> To examine this effect, we performed a set of simulations where we placed hydrogen atoms at the interfaces at various concentrations and performed structural relaxation simulations using the conjugate gradient scheme.

The work of separation ( $W_{\text{sep}}$ ), as introduced by Finnis et al.<sup>89</sup> is vital for quantifying the interfacial adhesion.  $W_{\text{sep}}$  is defined as the reversible work needed to separate an interface into two free surfaces, which is a measure of the strength of the interfaces<sup>89</sup> and calculated as:

$$W_{\text{sep}} = \sigma_{\text{Fe-sv}} + \sigma_{\text{Fe}_3\text{C-sv}} - \sigma_{\text{Fe/Fe}_3\text{C}}$$

$$= (E_{\text{Fe}} + E_{\text{Fe}_3\text{C}} - E_{\text{Fe/Fe}_3\text{C}})/2A$$

where,  $\sigma_{\text{Fe-sv}}$ ,  $\sigma_{\text{Fe}_3\text{C-sv}}$  are the solid-vapor surface energies, and  $\sigma_{\text{Fe/Fe}_3\text{C}}$  is the interface energy;  $E_{\text{Fe}}$  and  $E_{\text{Fe}_3\text{C}}$  are the total energies for the iron, cementite slab, respectively.  $E_{\text{Fe/Fe}_3\text{C}}$  is the total energy of the slab model with interfaces, and  $A$  is the interfacial area.

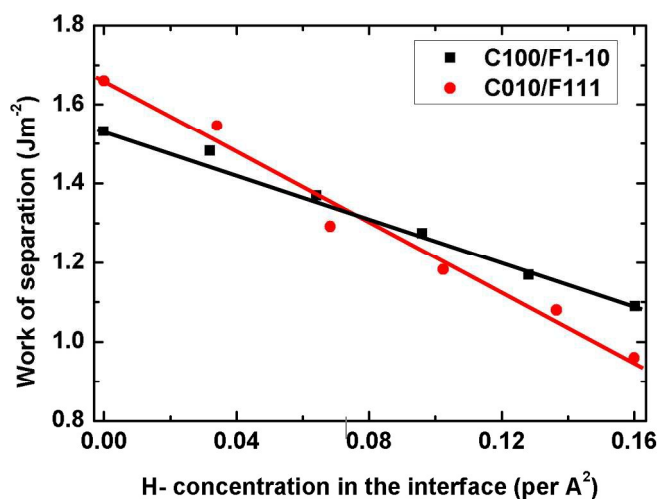


Fig. 8. Work of separation as a function of hydrogen concentration at the C100/F1 $\bar{1}$ 0 and C010/F111 Bagaryatskys' interfaces. C and F stands for cementite and ferrite surfaces, respectively.

We calculated  $W_{\text{sep}}$  for both of the BI interfaces at different hydrogen concentrations. Fig. 8 represents the relation between  $W_{\text{sep}}$  and hydrogen concentrations at the interfaces. Note that the reported  $W_{\text{sep}}$  values do not account for the effect of uncertainty stemming from different arrangement of hydrogens. In the current approach, we begin with a random placement of hydrogens and rely on the optimizer to fully relax and minimize the structure. However, the optimizer could only ensure us to provide the nearby local minimum for a given initial geometry and not the global minimum. Alternatively, one could start with "n" different starting configurations and aim to arrive at an estimate of uncertainty by fully relaxing them. Since, the uncertainty thus calculated would still not reflect the true measure of it as there is no way to ensure that one has tried all possible arrangements of hydrogens. Consequently, our intent in Fig. 8 is not to provide a quantitative measure of  $W_{\text{sep}}$  instead to demonstrate qualitatively the trend in  $W_{\text{sep}}$  with increasing hydrogens at the interface. One can see that in Fig. 8 for both of the interfacial configurations,  $W_{\text{sep}}$  decreases with the increasing hydrogen concentration at the interfaces, which indicates the weakening of the interfaces—i.e. lower energy is needed to cleave the interface into two surfaces. This finding corroborates with the observation of the hydrogen induced decohesion at the interfaces.<sup>25</sup> Wang and co-workers<sup>90</sup> study on  $\text{Cu}/\text{Al}_2\text{O}_3$  interfaces also revealed hydrogen-assisted reduction in  $W_{\text{sep}}$ .

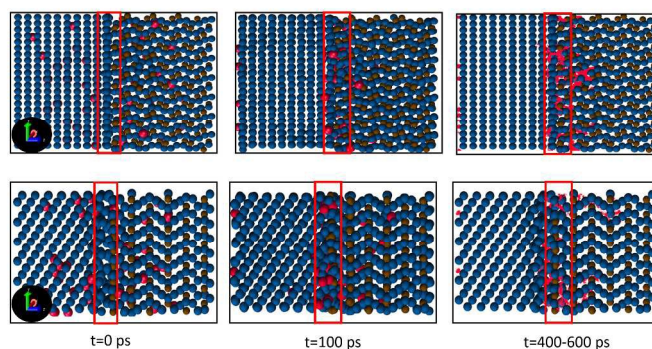


Fig. 9. Diffusivity and segregation of hydrogen at Bagaryatskys' Interfaces at  $t=0$ ps,  $t=100$ ps and  $t=400-600$ ps. Top panel:

C100/F110 and bottom panel: C010/F111. Color scheme: equilibrated hydrogen trajectories (red dots), hydrogen (red), carbon (ochre), and iron (blue).

Furthermore, hydrogen diffusion kinetics were studied in ferrite-cementite interface geometries. Twenty hydrogen atoms were randomly placed in each of the phases, and MD simulations were performed. The structural relaxation simulations followed by the NVT-MD simulations were performed at 500K temperature. Fig. 9 shows the evolution of the diffusivity of hydrogen atoms at 0ps, 100ps and the trajectory of equilibrated hydrogen atoms (shown as red dots) for 400-600ps at both interfaces. During the NVT-MD simulation, hydrogen atoms diffuse towards the interface from both phases and hydrogen accumulation is observed at the interface. The higher hydrogen diffusion coefficient at the ferrite phase facilitates the diffusion of hydrogen atoms to the interface at an expedited rate, while hydrogen segregation from the cementite phase to the interface takes place at a slower rate. Hanada *et al.*<sup>91</sup> reported that hydrogen atoms diffusing through the ferrite phase are being attracted to the cementite precipitators due to the negative gradient of the trapping potential of the cementite. The stress field induced in the ferrite matrix by the cementite at the interface is also responsible for the hydrogen accumulation at the interfaces.<sup>91</sup> Our results on the hydrogen segregation at the interfaces are consistent with the experimental observation.<sup>91</sup> Diffusion coefficient of the hydrogen atoms—trapped at the interfaces—is found three order of magnitude slower than the bcc-iron phase. For example, diffusion coefficient of hydrogen atoms trapped at the C010/F111 interface is calculated as  $2.40 \times 10^{-13} \text{ ms}^{-2}$ . Since interfaces act as a strong trap site for the hydrogen, we did not observe any hydrogen atoms to cross the interface from either of the phases.

## 5. Conclusions

We employed the Fe/C/H ReaxFF force field to explore experimentally observed phenomenon of hydrogen interaction with pure and defective  $\alpha$ -iron and with two types of Bagarytsky interfaces (BI) between the ferrite and cementite phases. ReaxFF simulations reasonably predict the diffusion coefficients of hydrogen in the  $\alpha$ -iron and Fe<sub>3</sub>C phases and hydrogen trapping at nanovoids. The prediction of phase dependent hydrogen diffusivity and hydrogen segregation at the interfaces agrees with experimental observations. The values of predicted hydrogen diffusion coefficient in three different phases follows a sequence of  $D_{\alpha\text{-iron}} > D_{\text{Fe}_3\text{C}} > D_{\text{interfaces}}$ . The Grand Canonical Monte Carlo (GCMC) simulation demonstrates the ability of the ReaxFF method in describing vacancy cluster formation and the growth of nanovoids. ReaxFF captures the phenomenon of hydrogen-induced decohesion type failures at the interfaces. Increase in hydrogen concentration at the interfaces reduces the work of separation, suggesting the possibility of crack propagation along the interfaces. Overall, the simulation results obtained in this study demonstrates that the Fe/C/H force field can satisfactorily describe hydrogen, vacancy, ferrite, and cementite interactions, which encourages us to extend our studies towards other aspects of hydrogen embrittlement using ReaxFF. Investigations are underway to explore the effect of hydrogen on the mechanical properties of iron nanowire and crack propagation behavior in  $\alpha$ -iron in the presence of hydrogen and precipitator interface. Most importantly, the present work highlights the transferability of the Fe/C/H force field that is trained against the data for describing Fischer-Tropsch catalysis to materials' characterization and emphasizes ReaxFF force field validation as a prerequisite while engaging ReaxFF capability for its unique strength to enable investigations of the effect of chemistry on the

mechanical properties of the material. Additional work is in progress to extend the length scales of reactive MD to hundreds of nanometers by using an adaptive hybrid force field scheme that involves a computationally intensive ReaxFF reactive force field description for the complex surface chemistry and computationally less expensive Tersoff or EAM potential to adequately describe the mechanical properties of the material.

## Acknowledgments

This work was supported by the Corporate Strategic Research, ExxonMobil Research and Engineering, Clinton, NJ. We like to thank Srinivasan Rajagopalan, Neeraj Thirumalai, and Lili Gai for useful comments and discussions.

## Notes and References

- <sup>a</sup>Summer Intern, ExxonMobil Research and Engineering, Annandale, New Jersey, 08801, USA  
<sup>b</sup>Department of Mechanical and Nuclear Engineering, The Pennsylvania State University, University Park, PA 16802, USA  
<sup>c</sup>RxFF Consulting, LLC, State College, PA 16801, USA  
<sup>d</sup>ExxonMobil Research and Engineering, Annandale, New Jersey, 08801, USA  
<sup>e</sup>Email: [sumathy.aman@exxonmobil.com](mailto:sumathy.aman@exxonmobil.com), Phone: (908) 730-2512, Fax: (908) 730-3323  
<sup>f</sup>Electronic supplementary information (ESI) available. See DOI:
- 1 T. Doshida, H. Suzuki, K. Takai, N. Oshima and T. Hirade, *ISIJ Int.*, 2012, **52**, 198–207.
  - 2 J. Song and W. A. Curtin, *Acta Mater.*, 2011, **59**, 1557–1569.
  - 3 J. Song and W. A. Curtin, *Nat. Mater.*, 2013, **12**, 145–151.
  - 4 S. P. Lynch, *Hydrog. Eff. Mater. Behav. Corros. Deform. Interact.*, 2003, 449–466.
  - 5 Y. Fukai, *The metal-hydrogen system: basic bulk properties*, Springer Science & Business Media, 2006, vol. 21.
  - 6 M. Nagumo, *Mater. Sci. Technol.*, 2004, **20**, 940–950.
  - 7 A. Pundt and R. Kirchheim, *Annu. Rev. Mater. Res.*, 2006, **36**, 555–608.
  - 8 J. P. Hirth, *Metall. Trans. A*, 1980, **11**, 861–890.
  - 9 A. Rajabipour and R. E. Melchers, *Int. J. Hydrog. Energy*, 2015, **40**, 9388–9399.
  - 10 M. Nagumo, T. Tamaoki and T. Sugawara, *Hydrog. Eff. Mater. Behav. Corros. Deform. Interact. NR Moody AW Thompson RE Ricker GW Was RH Jones Eds Miner. Met. Mater. Soc. N. Y.*, 2002, 999–1008.
  - 11 C. D. Beachem, *Metall. Trans.*, 1972, **3**, 441–455.
  - 12 H. K. Birnbaum and P. Sofronis, *Mater. Sci. Eng. A*, 1994, **176**, 191–202.
  - 13 A. R. Troiano, *Trans ASM*, 1960, **52**, 54–80.
  - 14 J. G. Morlet, H. H. Johnson and A. R. Troiano, *A new concept of hydrogen embrittlement in steel*, Wright Air Development Center, Air Research and Development Command, United States Air Force, 1957.
  - 15 R. A. Oriani, *Acta Metall.*, 1970, **18**, 147–157.
  - 16 H. C. Rogers, *Science*, 1968, **159**, 1057–1064.
  - 17 K. H. Lo, C. H. Shek and J. K. L. Lai, *Mater. Sci. Eng. R Rep.*, 2009, **65**, 39–104.
  - 18 H. Momida, Y. Asari, Y. Nakamura, Y. Tateyama and T. Ohno, *Phys. Rev. B*, 2013, **88**, 144107.
  - 19 J. L. Lee and J. Y. Lee, *Met. Sci.*, 1983, **17**, 426–432.
  - 20 W. Y. Choo and J. Y. Lee, *J. Mater. Sci.*, 1982, **17**, 1930–1938.
  - 21 S. L. I. Chan and J. A. Charles, *Mater. Sci. Technol.*, 1986, **2**, 956–962.
  - 22 V. P. Ramunni, T. D. P. Coelho and P. E. V. de Miranda, *Mater. Sci. Eng. A*, 2006, **435–436**, 504–514.
  - 23 S. M. Lee and J. Y. Lee, *Acta Metall.*, 1987, **35**, 2695–2700.
  - 24 H. G. Lee and J.-Y. Lee, *Acta Metall.*, 1984, **32**, 131–136.
  - 25 H.-L. Lee and S. Lap-Ip Chan, *Mater. Sci. Eng. A*, 1991, **142**, 193–201.
  - 26 S. Fujita and Y. Murakami, *Metall. Mater. Trans. A*, 2013, **44**, 303–322.

- 27 M. Wen, X.-J. Xu, S. Fukuyama and K. Yokogawa, *J. Mater. Res.*, 2001, **16**, 3496–3502.
- 28 A. Ramasubramaniam, M. Itakura, M. Ortiz and E. A. Carter, *J. Mater. Res.*, 2008, **23**, 2757–2773.
- 29 R. Nazarov, T. Hickel and J. Neugebauer, *Phys. Rev. B*, 2014, **89**, 144108.
- 30 D. Tanguy and M. Mareschal, *Phys. Rev. B*, 2005, **72**, 174116.
- 31 D. E. Jiang and E. A. Carter, *Phys. Rev. B*, 2004, **70**, 064102.
- 32 B. Irigoyen, R. Ferullo, N. Castellani and A. Juan, *J. Phys. Appl. Phys.*, 1996, **29**, 1306.
- 33 M. E. Pronsato, C. Pistonesi and A. Juan, *J. Phys. Condens. Matter*, 2004, **16**, 6907.
- 34 Y. Tateyama and T. Ohno, *Phys. Rev. B*, 2003, **67**, 174105.
- 35 Y. A. Du, J. Rogal and R. Drautz, *Phys. Rev. B*, 2012, **86**, 174110.
- 36 L. Ismer, T. Hickel and J. Neugebauer, *Phys. Rev. B*, 2010, **81**, 094111.
- 37 U. Khalilov, G. Pourtois, A. C. T. van Duin and E. C. Neyts, *J. Phys. Chem. C*, 2012, **116**, 21856–21863.
- 38 Q. Zhang, T. Çağın, A. van Duin, W. A. Goddard III, Y. Qi and L. G. Hector Jr, *Phys. Rev. B*, 2004, **69**, 045423.
- 39 B. V. Merinov, J. E. Mueller, A. C. T. van Duin, Q. An and W. A. Goddard, *J. Phys. Chem. Lett.*, 2014, 4039–4043.
- 40 C. Zou, A. C. T. van Duin and D. C. Sorescu, *Top. Catal.*, 2012, **55**, 391–401.
- 41 J. Tersoff, *Phys. Rev. Lett.*, 1988, **61**, 2879–2882.
- 42 D. W. Brenner, *Phys. Rev. B*, 1990, **42**, 9458–9471.
- 43 T. Liang, Y. K. Shin, Y.-T. Cheng, D. E. Yilmaz, K. G. Vishnu, O. Verners, C. Zou, S. R. Phillpot, S. B. Sinnott and A. C. T. van Duin, *Annu. Rev. Mater. Res.*, 2013, **43**, 109–129.
- 44 A. C. Van Duin, A. Strachan, S. Stewman, Q. Zhang, X. Xu and W. A. Goddard, *J. Phys. Chem. A*, 2003, **107**, 3803–3811.
- 45 K. Chenoweth, A. C. T. van Duin and W. A. Goddard, *J. Phys. Chem. A*, 2008, **112**, 1040–1053.
- 46 A. C. Van Duin, S. Dasgupta, F. Lorant and W. A. Goddard, *J. Phys. Chem. A*, 2001, **105**, 9396–9409.
- 47 M. R. LaBrosse, J. K. Johnson and A. C. T. van Duin, *J. Phys. Chem. A*, 2010, **114**, 5855–5861.
- 48 S. Cheung, W.-Q. Deng, A. C. T. van Duin and W. A. Goddard, *J. Phys. Chem. A*, 2005, **109**, 851–859.
- 49 W. J. Mortier, S. K. Ghosh and S. Shankar, *J. Am. Chem. Soc.*, 1986, **108**, 4315–4320.
- 50 O. Verners and A. C. T. van Duin, *Surf. Sci.*, 2015, **633**, 94–101.
- 51 M. M. Islam, A. Ostadhossein, O. Borodin, A. T. Yeates, W. W. Tipton, R. G. Hennig, N. Kumar and A. C. T. van Duin, *Phys. Chem. Chem. Phys.*, 2015, **17**, 3383–3393.
- 52 A. Ostadhossein, E. D. Cubuk, G. A. Tritsarlis, E. Kaxiras, S. Zhang and A. C. T. van Duin, *Phys. Chem. Chem. Phys.*, 2015.
- 53 C. Zou, Y. K. Shin, A. C. T. van Duin, H. Fang and Z.-K. Liu, *Acta Mater.*, 2015, **83**, 102–112.
- 54 C. Zou and A. V. Duin, *JOM*, 2012, **64**, 1426–1437.
- 55 M. M. Islam, V. S. Bryantsev and A. C. T. van Duin, *J. Electrochem. Soc.*, 2014, **161**, E3009–E3014.
- 56 D.-C. Yue, T.-B. Ma, Y.-Z. Hu, J. Yeon, A. C. van Duin, H. Wang and J. Luo, *Langmuir*, 2015, **31**, 1429–1436.
- 57 M. F. Russo Jr. and A. C. T. van Duin, *Nucl. Instrum. Methods Phys. Res. Sect. B Beam Interact. Mater. At.*, 2011, **269**, 1549–1554.
- 58 S. G. Srinivasan, A. C. T. van Duin and P. Ganesh, *J. Phys. Chem. A*, 2015, **119**, 571–580.
- 59 L. S. I. Liyanage, S.-G. Kim, J. Houze, S. Kim, M. A. Tschopp, M. I. Baskes and M. F. Horstemeyer, *Phys. Rev. B*, 2014, **89**, 094102.
- 60 W. G. Marshall, G. D. Pricea and I. G. Wooda, *Earth Planet. Sci. Lett.*, 2002, **203**, 575.
- 61 F. H. Herbstein and J. Smuts, *Acta Crystallogr.*, 1964, **17**, 1331–1332.
- 62 C. Kittel, *Introduction to Solid State Physics*, Wiley, 2004.
- 63 J. Li, H. K. Mao, Y. Fei, E. Gregoryanz, M. Erements and C. S. Zha, *Phys. Chem. Miner.*, 2002, **29**, 166–169.
- 64 B.-J. Lee and J.-W. Jang, *Acta Mater.*, 2007, **55**, 6779–6788.
- 65 D. C. Sorescu, *Catal. Today*, 2005, **105**, 44–65.
- 66 P. Söderlind, L. H. Yang, J. A. Moriarty and J. M. Wills, *Phys. Rev. B*, 2000, **61**, 2579.
- 67 C. Domain and C. S. Becquart, *Phys. Rev. B*, 2001, **65**, 024103.
- 68 P. A. Korzhavyi, I. A. Abrikosov, B. Johansson, A. V. Ruban and H. L. Skriver, *Phys. Rev. B*, 1999, **59**, 11693.
- 69 E. Hayward and C.-C. Fu, *Phys. Rev. B*, 2013, **87**, 174103.
- 70 S. M. Myers, P. M. Richards, W. R. Wampler and F. Besenbacher, *J. Nucl. Mater.*, 1989, **165**, 9–64.
- 71 Y. K. Shin, H. Kwak, C. Zou, A. V. Vasenkov and A. C. T. van Duin, *J. Phys. Chem. A*, 2012, **116**, 12163–12174.
- 72 W. C. Chiou Jr. and E. A. Carter, *Surf. Sci.*, 2003, **530**, 88–100.
- 73 G. Kresse and J. Hafner, *Phys. Rev. B*, 1993, **48**, 13115.
- 74 G. Kresse and J. Furthmüller, *Phys. Rev. B*, 1996, **54**, 11169.
- 75 P. E. Blöchl, *Phys. Rev. B*, 1994, **50**, 17953.
- 76 A. C. van Duin, B. V. Merinov, S. S. Han, C. O. Dorso and W. A. Goddard Iii, *J. Phys. Chem. A*, 2008, **112**, 11414–11422.
- 77 K. Kiuchi and R. B. McLellan, *Acta Metall.*, 1983, **31**, 961–984.
- 78 H. Z. Fang, S. L. Shang, Y. Wang, Z. K. Liu, D. Alfonso, D. E. Alman, Y. K. Shin, C. Y. Zou, A. C. T. van Duin, Y. K. Lei and G. F. Wang, *J. Appl. Phys.*, 2014, **115**, 043501.
- 79 L. K. Mansur, *J. Nucl. Mater.*, 1994, **216**, 97–123.
- 80 G. R. Odette, M. J. Alinger and B. D. Wirth, *Annu. Rev. Mater. Res.*, 2008, **38**, 471–503.
- 81 Y. Fan, A. Kushima, S. Yip and B. Yildiz, *Phys. Rev. Lett.*, 2011, **106**, 125501.
- 82 C.-C. Fu, J. D. Torre, F. Willaime, J.-L. Bocquet and A. Barbu, *Nat. Mater.*, 2005, **4**, 68–74.
- 83 L. K. Mansur, *Kinet. Nonhomogeneous Process. Pract. Introd. Chem. Biol. Phys. Mater. Sci. GR Freeman Ed Wiley N. Y.*, 1987, 377–463.
- 84 T. P. Senftle, M. J. Janik and A. C. T. van Duin, *J. Phys. Chem. C*, 2014, **118**, 4967–4981.
- 85 M. Eldrup and B. N. Singh, *J. Nucl. Mater.*, 2003, **323**, 346–353.
- 86 M. Iino, *Metall. Trans. A*, 1978, **9**, 1581–1590.
- 87 A. Arya and E. A. Carter, *J. Chem. Phys.*, 2003, **118**, 8982–8996.
- 88 D. S. Zhou and G. J. Shiflet, *Metall. Trans. A*, 2013, **23**, 1259–1269.
- 89 M. W. Finnis, *J. Phys. Condens. Matter*, 1996, **8**, 5811.
- 90 X.-G. Wang, J. R. Smith and M. Scheffler, *Phys. Rev. B*, 2002, **66**, 073411.
- 91 H. Hanada, T. Otsuka, H. Nakashima, S. Sasaki, M. Hayakawa and M. Sugisaki, *Scr. Mater.*, 2005, **53**, 1279–1284.